41st AIAA/ASME/ASEE Joint Propulsion Conference, Tucson AZ, July 2005   AIAA 2005-3908

EVALUATION OF HOMOLOGOUS SERIES OF NORMAL-ALKANES AS HYBRID ROCKET FUELS

M. Arif Karabeyoglu[*], Brian J. Cantwell[‡], and Jose Stevens[¶]

Stanford University
Stanford, CA
and
Space Propulsion Group Inc.
Sunnyvale, CA

Abstract

The liquid layer hybrid combustion theory which was developed to predict the regression rate behavior of hybrid rocket fuels burning by forming a liquid layer on their surfaces has been improved. In the enhanced version of the theory, the regression rate equations are cast in a non-dimensional format, normalized by the classical regression rate, and a universal law for the non-dimensional regression rate has been derived. Comprehensive prediction methods for the surface temperature have been developed for the subcritical and the supercritical operating conditions for the molten fuel. Note that each regime is quite different in terms of the underlying surface phenomenon. In the subcritical operation, the temperature is dictated by the physical phase transformation process whereas in the supercritical case, pyrolysis chemistry governs the surface phenomenon. The enhanced theory has been applied to the homologous series of normal alkanes (C_2H_{2n+2}) which are fully saturated hydrocarbons with varying numbers of carbon atoms. It has been demonstrated that the regression rate predicted by the theory matches the data obtained from the motor tests with reasonable accuracy. The motor test data used in the comparison was based on a wide range of practical fuel systems composed of n-alkane molecules including liquid pentane ($n=5$), paraffin waxes ($n=28-32$), PE waxes ($n=60-80$) and, finally, the high density polyethylene polymer ($n > 100,000$).

1. Nomenclature

A_{cc} :	Evaporation equation coefficient
a_{ent} :	Entrainment coefficient
a_l :	Average gray body absorption coefficient in the liquid phase
a_p :	Pyrolysis reaction rate coefficient for the Arrhenius form
a_t :	Thickness parameter
B , B_g :	Blowing parameter and evaporation blowing parameter
B_1, B_2, B_3 :	Thermal variables
C :	Specific heat
C_{B1}, C_{B2} :	Blowing correction coefficients
C_f, C_{fo} :	Skin friction coefficient with and without blowing
C_H, C_{Ho} :	Stanton number with and without blowing
E_a :	Activation energy for pyrolysis
E_v :	Activation energy for viscous flow
F_r :	Heat transfer correction factor for surface roughness
G , G_{ox} :	Local, instantaneous mass flux, oxidizer mass flux
h :	Melt layer thickness
h_m, h_e :	Effective heats
h_s, h_b :	Enthalpies at the surface and flame
h_v :	Effective heat of gasification
I , I_p :	Reaction layer integrals
K :	Entrainment parameter coefficient
k :	Boltzmann's constant, reaction exponent
k_p :	Pyrolysis reaction rate coefficient
L_m, L_v :	Latent heat of melting and vaporization
L_{v,T_b} :	Latent heat of vaporization at the normal boiling temperature
M_{cr} :	Critical molecular weight for entanglement

[*] President/CTO, Space Propulsion Group Inc., Consulting Professor, Stanford University, Member AIAA
[‡] Chairman and Edward C. Wells Professor, Dept. of Aeronautics and Astronautics, Stanford University, Fellow AIAA
[¶] Senior Engineer, Space Propulsion Group Inc.

American Institute of Aeronautics and Astronautics

M_m :	Molecular weight of the monomer
M_w :	Molecular weight of the alkane C_nH_{2n+2}
$\dot{m}_{cond}$:	Condensation mass flux into fuel surface
$\dot{m}_{ent}$:	Entrainment component of mass flux from fuel surface
$\dot{m}_{evap}$:	Evaporation mass flux from fuel surface
$\dot{m}_v$:	Net vaporization mass flux from fuel surface
N_a :	Avogadro's number
n :	Carbon number
n_e :	Effective carbon number of the pyrolysis products
n_o :	Offset carbon number for the ABC prediction method
n_σ :	Number density of the molecules on unit surface
$(O/F)_f$:	Oxidizer to fuel ratio at the flame
PD :	Polydispersity
P_a :	Pressure for normal boiling temperature, 1 atm
P_c :	Chamber pressure
P_{cr} :	Critical pressure
P_f :	Partial pressure of fuel at the surface
$\dot{Q}_r$, $\dot{Q}_c$:	Radiative and convective heat flux at the surface
$\dot{Q}_s$:	Total heat flux at the surface
q_p :	Heat of pyrolysis
R_{ent} :	Entrainment parameter
R_{hv} , R_{he} :	Ratio of effective heat of gasifications for entrainment and vaporization
R_l :	Ratio of thermal to radiative thickness in the liquid
R_u :	Universal gas constant
$\dot{r}$:	Total regression rate
$\dot{r}_{cl}$:	Regression rate predicted by classical theory
$(\dot{r}_{cl})_{ref}$:	Regression rate for the HDPE polymer
$\dot{r}_{ent}$, $\dot{r}_v$:	Entrainment and vaporization components of the regression rate
$2s$:	Number of quadratic terms among which the activation energy is distributed
T :	Temperature
T_a :	Ambient temperature
T_b :	Normal boiling temperature
T_g :	Average gas phase temperature, glass transition temperature
T_m , T_s :	Melting and surface temperatures

T_{melt} :	Effective temperature of the melt layer
T_p :	Temperature at which the pyrolysis reactions start
T_{solid} :	Effective temperature of the solid
u :	Temperature gradient variable
Y :	Quantity predicted by the ABC method
x_p , x_l , x_s :	Normal distance in the pyrolysis, liquid and solid zones
Y_f :	Fuel mass fraction
Y_{fb} :	Fuel mass fraction at the flame
Y_{fs} :	Fuel mass fraction at the surface
$Y_o , Y_{\infty,0}$:	ABC method parameters
z :	Axial distance along the port
α :	Mass flux exponent
α_1 , α_2 :	Reaction layer thickness variables
β :	Thickness exponent, ABC prediction method parameter
δ_l :	Characteristic thermal thickness in liquid
δ_p :	Thickness of the pyrolysis layer
δ_r :	Thickness of the radiation absorption layer $(1/a_l)$
$\Delta H_{f,298}^{IG}$:	Heat of formation of the ideal gas at 298 K
$\Delta H_{f,Ta}^{s}$:	Heat of formation of the solid at ambient temperature
Δh :	Enthalpy difference between the flame and the surface
$\Delta Y_o , \Delta Y_\infty$:	ABC method parameters
ε :	Activation energy for evaporation per molecule
ϕ , ϕ_{ent} :	Non-dimensional regression rate parameters, total and entrainment
ϕ_v , ϕ_{cl} :	Non-dimensional regression rate parameters, vaporization and classical
γ :	ABC method parameter
κ :	Thermal diffusivity
λ_l :	Thermal conductivity
μ :	Viscosity
μ_{mol} :	Molecular mass
μ_{Tg} , μ_{cr} :	Glass transition and critical viscosities
$\overline{\upsilon}$:	Oscillation frequency of the molecules in the liquid phase
θ :	Non-dimensional temperature
ρ :	Density
ρ_s :	Solid density
σ :	Surface tension

ψ :   Non-dimensional thickness parameter

ζ :   Temperature difference variable

Subscripts:
ent :   Entrainment
g :   Gas
l :   Liquid
ox :   Oxidizer
s: Surface

Superscripts:
^ :   Molar based quantity
- :   Non-dimensional quantity

2. Introduction

Despite their safety and cost advantages over solid and liquid systems, conventional hybrid rockets possess one very significant shortcoming: very low fuel regression rates. For many practical applications, this leads to a complex, multi-port grain design such as the commonly used wagon wheel configuration. The multi-port design presents serious shortcomings, which significantly degrade the overall performance, reliability and cost effectiveness of a hybrid propulsion system.

Fundamentally, the limit on regression rate for conventional hybrid fuels is set by the physical phenomena of heat and mass transfer from the relatively remote flame zone to the fuel surface[1]. Heat transfer to the fuel surface is further reduced by the well-known "Blocking Effect" which is induced by the radial blowing of the gas from the fuel surface at relatively high velocities. As a consequence, the regression rates of modern hybrids that utilize polymers as the fuel are much lower than conventional solid rocket burning rates.

So far many techniques directed toward increasing the heat transfer to the fuel surface have been suggested or tried to improve the fuel regression rate of hybrid rocket systems. Unfortunately, all of these methods suffer from important shortcomings. We believe that a natural and effective methodology to increase the regression rate is to formulate a hybrid fuel that will generate mass transfer by mechanical means in addition to the mass transfer by direct gasification from the fuel surface. For materials forming a low viscosity melt layer on their burning surfaces, the mechanical mass transfer will take place by the entrainment of liquid droplets into the gas stream. An obvious class of entraining substances includes liquids or gases at standard conditions, which are frozen to form solids (i.e. solid cryogenic hybrids). However it is clear that the same internal ballistic behavior can be experienced by materials that are solids at standard conditions if they form a low viscosity melt layer at the combustion surface.

In fact, increased regression rates by several hundred percent have been observed with solid cryogenic hybrids by researchers at the Air Force Research Laboratory (AFRL)[2,3,4] and ORBITEC[5,6]. The AFRL program was concentrated on burning several frozen organic liquids including normal pentane with gaseous oxygen in a small test motor. As discussed in references 2 and 3, the measured regression rates for cryogenic pentane are 3-4 times larger than the reported regression rates for the conventional fuel, HTPB, under the same oxidizer mass flux condition.

Similarly, ORBITEC conducted tests using solidified kerosene and methane with gaseous oxygen and solidified oxygen with gaseous methane (i.e. a reverse hybrid configuration) with small AFRL scale motors. In the process of developing a production technique for frozen methane fuel grains, ORBITEC has also performed a limited number of tests with a low molecular weight paraffin wax. The oxidizer mass fluxes corresponding to the measured regression rates for the paraffin tests were not reported. Similar to the AFRL results, solid kerosene and methane showed very high burning rates relative to the polymeric classical hybrids. However regression rate data for methane and kerosene is not adequate to make a meaningful comparison with the other well studied hybrid fuels.

The main conclusion from these various experiments is that the regression rates for cryogenic propellants are many times higher than for conventional hybrids. This observation cannot be explained by a lower heat of vaporization, which is insufficient to account for the observed regression rate increase. Recall that in the classical regression rate expression[1, 7], the heat of vaporization is incorporated in the blowing parameter, B, raised to a power 0.32. Thus reducing the effective heat of gasification would only cause a modest increase in the regression rate (30-50 %) over conventional systems rather than the observed increases of 300-400%. A different mechanism is clearly indicated.
A regression rate model has been developed for these liquefying propellants[8, 9, 10]. In addition to the classical gasification, a mass transfer mechanism involving the entrainment of liquid droplets from the melt layer has been postulated. As demonstrated in references 8 and 10, droplet formation is due to liquid layer instabilities, which result from the high velocity gas flow in the port. A schematic of the model for entrainment is shown in Figure 1.

The liquid layer theory has been implemented[8, 11, 12] to formulate various non-cryogenic paraffin-based fuels which have demonstrated burn rates that are 3-4 times faster than the well known classical fuel HTPB. A specific formulation, SP-1a, with the baseline paraffin wax FR 5560 (with a melting temperature of approximately 70 C) has been tested extensively with various oxidizers (i.e. GOX, LOX and N_2O) using motors up to 6,000 lbf of nominal thrust[11, 13].

The homologous series of normal alkanes is a group of fully saturated, straight chain hydrocarbons with the chemical formula C_nH_{2n+2}. Each member of the series is identified by the carbon number n, which ranges from 1 (methane) all the way up to High Density Polyethylene (HDPE) polymer with very large carbon numbers. The high heat of combustion (due to the high hydrogen to carbon ratio), low cost, availability and chemical inertness characteristics of n-alkanes makes them ideal fuels for combustion systems. A short list of materials that are primarily made out of n-alkanes, that are of interest in propulsion applications, are: methane (*n=1*), pentane (*n=5*), paraffin waxes (*n=16-40*), PE waxes (*n=40-300*) and HDPE polymer (*n>300*). Note that the specified ranges for the carbon numbers of the waxes is arbitrary and they are listed here to give a general idea. We would like to emphasize that a large fraction of the fast burning liquefying hybrid fuels tested to date are also either pure normal alkanes such as pentane or mixtures of n-alkanes such as paraffin waxes.

The purpose of this paper is to enhance the liquid layer combustion theory such that it can be used to predict the regression rate performance of a selected fuel and apply it to the homologous series of normal alkanes. We first summarize the current state of the liquid layer theory, and give the set of equations that can be solved to determine the regression rate. Next we set the problem in a non-dimensional format and derive an approximate closed form solution for the non-dimensional regression rate as a function of the entrainment parameter which is an empirical relation that correlates the entrainment mass transfer to the material properties of the fuel. The surface temperature is an important variable that needs to be determined since the thermophysical properties of the fuel depends strongly on the effective temperature of the melt layer. The surface temperature is dictated by some complex physical and/or chemical phenomena depending on the critical state of the molten fuel under the operating conditions. We have derived formulas for the surface temperature for subcritical and supercritical conditions. For the subcritical case the temperature is determined by a physical process controlled by the phase change (evaporation), whereas for the supercritical case the

temperature depends on the chemical process of pyrolysis.

In the next section, we summarize the important property prediction methods for the normal alkanes that are needed to calculate the regression rate using the liquid layer combustion theory. Finally the theory is applied to the homologous series of n-alkanes and the theory predictions are compared to the motor test data for various paraffinic fuels.

3. Liquid Layer Hybrid Combustion Theory

In this section we summarize the liquid layer theory that has been developed in references 8, 9 and 10 and has been used to successfully predict the regression rates of fuels that form a liquid layer on their burning surfaces. Following the summary of the present state of the liquid layer theory, we will introduce several improvements.

Due to the complexity of the problem, the modeling has been performed in three stages. In the first stage, the requirements for the formation of a melt layer on the fuel grain has been investigated. In the second stage, the linear stability of a thin melt layer under the strong shear of a gas flow has been considered[8, 9]. Later the linear stability results has been linked to the entrainment of liquid droplets with use of some experimental results and some semi-empirical relations developed in the nuclear engineering and film cooling literature. Eventually in the final stage, classical theory has been extended to the case of liquid droplet entrainment.

Film Thickness Estimation: In this stage a steady one dimensional thermal analysis has been conducted to estimate the film thickness formed on a burning slab under the combined heating by convection and radiation. In the derivation, it has been inherently assumed that the operation is subcritical and the surface temperature is dictated by the evaporation process. For the sake of simplicity, the thermophysical properties of the material both in the liquid phase and solid phase are assumed to be uniform. The effect of convection in the liquid layer was also ignored because of the small melt layer thicknesses for which the Reynolds numbers are relatively small (a couple of hundreds), and the temperature gradients are fairly large.

Under these simplifying assumptions the thermal analysis yields the following expression for the thickness of the melt layer[9, 11].

$$h = \delta_l \, \ln(1/\psi) \qquad (1a)$$

where the characteristic thermal thickness in the liquid phase is defined as $\delta_l = \kappa_l \rho_s / \dot{r} \rho_l$. The thickness parameter, ψ, which depends mainly on the thermophysical properties and radiative absorbtion character of the fuel and the nature of the heat transfer to the fuel surface can be found as a solution of the following nonlinear equation.

$$\psi = \frac{h_m (R_l - 1) + h_v (\dot{Q}_r / \dot{Q}_w) \, \psi^{R_l}}{h_e (R_l - 1) + h_v (\dot{Q}_r / \dot{Q}_w)} \qquad (1b)$$

Here the following definitions of the effective heating parameters are introduced for convenience.

$$h_m = L_m + C_s (T_m - T_a) \qquad (2a)$$

$$h_e = h_m + C_l (T_s - T_m) \qquad (2b)$$

$$h_v \equiv \frac{\dot{Q}_s}{\rho_s \dot{r}} = h_e + L_v (\dot{r}_v / \dot{r}) \qquad (2c)$$

The form of effective heat of gasification, h_v, given in Eq. 2c is slightly different than the expressions commonly encountered in the literature, since no heat is required to vaporize the material transported by means of entrainment .

Note that T_a, T_m, T_s are the ambient, melting and surface temperatures of the fuel, respectively. The surface temperature has been approximated by the normal boiling temperature of the fuel. This is a deficient assumption for many materials and will be relaxed based on the arguments introduced later in this paper. $\dot{Q}_r$ and $\dot{Q}_w$ are the radiative and total heat fluxes to the fuel surface, C_l and C_s are the average specific heats of the liquid and solid and L_m and L_v are the latent heats for melting and vaporization (at the surface temperature). Also note that $\dot{r}$ and $\dot{r}_v$ are the total and vaporization components of the regression rate. Another important parameter that appears in the thickness expression is the non-dimensional radiation parameter, R_l, which is defined as the ratio of the thermal thickness to the radiative thickness in the liquid phase.

$$R_l = \delta_l a_l \qquad (3)$$

Note that a_l is the average gray body absorption coefficient in the liquid phase.

An explicit solution for the algebraic nonlinear equation, Eq. 1b, for the general case could not be obtained. We focus on the following two limiting cases of practical interest.

1) $R_l \gg 1$: The absorption of the radiation in the liquid layer is very large. In this extreme case of an opaque liquid layer, all the radiative heat is absorbed at the liquid-gas interface. The thickness can be solved explicitly as

$$h = \delta_l \ln\left[1 + C_l (T_s - T_m)/h_m\right]. \qquad (4)$$

Note that all the thermophysical properties of the fuel material are lumped in the logarithmic term and the $\dot{Q}_r / \dot{Q}_c$ ratio[*] does not affect the thickness. Similarly the ratio of the regression rates $\dot{r}_v / \dot{r}$ does not appear in the thickness formula. This case is important for propellants that are loaded with strongly absorbing materials such as carbon black.

2) $R_l \ll 1$: In this other extreme, the absorption of the radiation in the liquid phase is small. Here the thickness of the thermal layer in the liquid is much smaller than the radiative thickness in the liquid and as a consequence all the radiative flux is absorbed in the solid. This case has practical importance for cryogenic hybrids such as pentane which were tested without a radiation absorption agent. The effect of the entrainment mass transfer on the thickness is also included in this formulation. Unlike the other extreme, in this case the film thickness depends on the ratio of the radiative heat flux to the convective heat flux and it can be expressed as

$$h = \delta_l \ln\left[1 + \frac{C_l (T_s - T_m)}{h_m - h_v (\dot{Q}_r / \dot{Q}_w)}\right]. \qquad (5)$$

Note that the dependence of the thickness on $\dot{r}_v / \dot{r}$ comes from the effective heat of gasification, h_v that appears explicitly in this formula and is defined in Eq. 2c. Note that an important common property of the regression rate expressions Eq. 4 and Eq. 5 is that the melt layer thickness is proportional to the characteristic thermal length of the liquid, δ_l, and thus inversely proportional to the regression rate.

$$h = \frac{a_t}{\dot{r}} \qquad (6)$$

Here the thickness parameter, a_t, has been introduced for convenience.

---

[*] Note that $\dfrac{\dot{Q}_r}{\dot{Q}_s} = \dfrac{\dot{Q}_r / \dot{Q}_c}{1 + \dot{Q}_r / \dot{Q}_c}$ where $\dot{Q}_c$ is the convective heat flux to the fuel surface.

$$a_t = \frac{\kappa_l \rho_s}{\rho_l} \ln\left(\frac{1}{\psi}\right) \tag{7}$$

Linear Stability Investigation: The hydrodynamic instability of the liquid film formed on the surface of a hybrid fuel grain is essential for the possibility of entrainment from the liquid interface. The stability of liquid layers under strong blowing conditions and relatively high liquid Reynolds numbers, which are encountered in hybrids has been studied and reported in Refs. 8 and 10. Here are the major conclusions from these studies:

- Even at very small film thicknesses there exists a finite range of amplified wave numbers, namely the layer is unstable over a finite range of wave numbers. The instabilities of this type were first discovered for thin water films in a wind tunnel by Craik[14] and they are called the "slow waves". These are generated by the interaction of the gas phase shear stresses acting on the liquid surface with the slope of the liquid layer surface.
- As the liquid layer Reynolds number (which is directly proportional to the local mass flux) increases, the amplification rate also increases. The Reynolds number also increases the most amplified wave number. This means that at higher gas flow velocities, the expected wavelengths of the instabilities are smaller.
- Both the surface tension and also the viscosity of the liquid have a stabilizing effect on the liquid film.

Liquid Entrainment Relationships: The linear stability treatment summarized in the previous section revealed that the melt layers typically encountered in hybrid applications could develop interfacial instabilities. Even though the existence of these linear instabilities is a necessary condition, it is not sufficient for the entrainment process to occur. Before entrainment of droplets can take place, the infinitesimal harmonic disturbances growing at the liquid-gas interface must conform into a non-harmonic waveform with a finite amplitude. The process of growth to a finite amplitude and eventually entrainment of droplets is a highly nonlinear phenomenon, which is extremely difficult to model. We bypass this difficult but critical step by using some empirical relations that are introduced in the existing literature for the entrainment from thin liquid films under strong shear forces exerted by a gas flow. As stated in the literature, one plausible mechanism for droplet entrainment from these thin films at large Reynolds numbers is through the formation of nonlinear "Roll Waves". As schematically indicated in Fig. 1, the droplets are drawn from the tips

of these nonlinear waves by the stresses exerted by the local gas flow.

The most relevant experimental work on entrainment is reported by Gater and L'Ecuyer in an early paper[15]. In this study, which was motivated to address the liquid injection requirements for film cooling applications, the entrainment rates from thin films of various liquids (including some hydrocarbons such as RP-1 and methanol) under strong gas flow were measured. The experiments were performed in a wind tunnel and some tests were executed with hot gas flow. The entrainment relationship suggested by Gater and L'Ecuyer, which is slightly modified in Ref. 9, can be further simplified to the following form to capture the scaling with the important parameters one would encounter in hybrid rocket applications.

$$\dot{m}_{ent} = \dot{r}_{ent} \rho_s = K' \frac{C_f G^{2\alpha} h^\beta \rho_l}{\mu_l \sigma} =$$
$$= K' \frac{C_f a_t^\beta \rho_l}{\mu_l \sigma} \frac{G^{2\alpha}}{\dot{r}^\beta} \tag{8}$$

Here $\dot{r}_{ent}$ is the entrainment portion of the regression rate, K is the empirical entrainment parameter constant and G is the local mass flux in the fuel port. Note that the entrainment regression rate is a combined function of the operational parameters such as the mass flux and the regression rate, and the liquid layer properties such as the viscosity, density and the thickness coefficient. For the Gater and L'Ecuyer scaling law, the dynamic pressure exponent, α, and the thickness exponent, β, are specified as 1.5 and 2, respectively.

We would like to note that no universally accepted entrainment scaling formula exists in the literature[16, 17, 18]. Different researchers suggested different functional forms for the entrainment mass transfer. We have decided to base our analysis on the Gater and L'Ecuyer formulation because of the wide range of experimental conditions they have tested and the reasonably broad class of materials they have used in their experiments. The development of a non-dimensional, universal formula for the entrainment mass transfer would be quite beneficial in the further enhancement of the liquid layer hybrid combustion theory.

We finally note that the moderate to high carbon number normal alkanes such as paraffin waxes have low critical pressures resulting in supercritical conditions for almost all practical operating regimes. Thus a surface separating the liquid phase from the vapor phase does not exist and the surface tension is not well defined. For this reason we will drop the

surface tension dependency and use the following form for the scaling law for the entertainment mass transfer.

$$\dot{m}_{ent} = \dot{r}_{ent} \rho_s = K'' \frac{C_f G^{2\alpha} h^{\beta} \rho_l}{\mu_l} =$$

$$= K'' \frac{C_f a_t^{\beta} \rho_l}{\mu_l} \frac{G^{2\alpha}}{\dot{r}^{\beta}} \qquad (9)$$

Even for the low carbon number materials such as pentane the surface tension at typical chamber pressures is fairly small and the variation in the surface tension of the liquid films within the homologous series has been proven to be quite limited. Thus Eq. 9 will also be used for the members of the series operating under subcritical conditions.

Modification of the Classical Theory for Entrainment: It has been shown in the previous sections that a liquid layer can be formed on the fuel grain and this liquid layer can be unstable over a reasonable range of parameters typical of hybrid operation. It is also indicated that the instabilities in the liquid layer may induce the entrainment of liquid droplets into the gas stream. The final phase of the development involves the modification of the classical hybrid boundary layer combustion theory for the possibility of entrainment mass transfer from the fuel grain.

The formation of the liquid layer instabilities and entrainment of liquid droplets require three major modifications in the classical hybrid combustion theory.

- The effective heat of gasification is reduced since the evaporation energy required for the fuel mass transfer from the surface is partly avoided by the mechanical entrainment of the liquid. The enthalpy difference between the flame and the surface is also reduced, since some of the reactants are now in liquid phase. It is estimated that, the reduction in the effective heat of gasification is more dominant than the change in the enthalpy difference. Thus, as a first approximation, we assume that the reduction in the flame enthalpy is negligible.

- The blocking factor, C_H / C_{Ho}, that modifies the convective heat flux to the surface is also altered

due to the presence of the two-phase flow. As a first approximation we ignore the effect of the liquid droplets on the momentum and energy transfer. Under this assumption the blocking factor can be expressed as a function of evaporation blowing parameter.

$$C_H / C_{Ho} = f\left(B_g\right)$$

The evaporation blowing parameter, B_g, only includes the gaseous phase mass transfer from the fuel surface. We assume that evaporation of the droplets released from the liquid surface into the gas stream does not take place beneath the flame sheet. This assumption is consistent with the flame sheet approximation, which is a standard one in hybrid combustion modeling. Moreover, it is a reasonable approximation for typical hybrid operating conditions that are characterized by high blowing rates, and thus low residence time of droplets between the liquid surface and the diffusion flame. However, we believe that a more rigorous treatment of the two-phase flow in the hybrid boundary layer will be an important step in the further improvement of the liquefying hybrid theory.

- The ripples formed on the liquid layer surface increase the surface roughness and the heat transfer from the flame front to the surface. This is predicted to be a smaller influence on the total regression rate compared to the first two factors.

In general, the total regression rate of a hybrid motor can be written as a sum of the evaporation regression rate that is generated by the vaporization of the liquid into the gas stream (or first thermal decomposition and later volatilization into the gas stream in the case of supercritical operation) and the entrainment regression rate, which is due to the mass transfer mechanically extracted from the liquid surface.

$$\dot{r} = \dot{r}_v + \dot{r}_{ent} \qquad (10)$$

For an arbitrary combination of the entrainment and evaporative mass transfer the energy balance at the liquid-gas interface is

$$\dot{r}_v + \left[R_{he} + R_{hv}\left(\dot{r}_v/\dot{r}\right)\right] \dot{r}_{ent} = F_r \frac{0.03\mu_g^{0.2}}{\rho_s}\left(1 + \dot{Q}_r/\dot{Q}_c\right)B \frac{C_H}{C_{Ho}} G^{0.8} z^{-0.2} \qquad (11)$$

where

$$R_{hv} = \frac{C_l(T_s - T_m)}{h_v} \quad \text{and} \quad R_{he} = \frac{h_m}{h_v}. \quad (12)$$

Here the non-dimensional energy parameters for entrainment (R_{he}) and vaporization (R_{hv}) are introduced because the material that is extracted through the entrainment mechanism possesses different heating histories (i.e. no heat of vaporization or pyrolysis is required for entrainment). We postulate that the effective heating in the liquid phase required for the fuel material which is going through the entrainment mass transfer mechanism reduces linearly as the vaporization component of the regression rate decreases. This extra complexity, which was ignored in the thickness estimation arguments, is introduced to capture the asymptotic behavior of regression rate in the entrainment-dominated region of operation. We would like to note that the effect of reduced liquid phase heating on the thickness at moderate entrainment conditions is small since the thickness presents a logarithmic dependence on the energy terms.

The roughness parameter, F_r, is introduced in the energy equation to account for the increased heat transfer by wrinkling of the liquid surface. It has been argued by Gater and L'Ecuyer[15] that the surface roughness decreases with increasing dynamic pressure of the gas flow. This argument is based on the observed reduction in the scale of the interfacial disturbances with increasing dynamic pressure. Note that this phenomenon is captured by the linear stability theory which shows decreasing wave length with increasing gas mass flux[8, 10]. The empirical formula for the roughness correction parameter suggested by Gater and L'Ecuyer can be expressed in terms of the operational parameters of the motor as

$$F_r = 1 + \frac{14.1 \; \rho_g^{0.4}}{G^{0.8}(T_g/T_s)^{0.2}}. \quad (13)$$

In this formula the units of mass flux and gas density are kg/m²-sec and kg/m³, respectively.

Ref. 9 gives a new curve fit expression for the blowing correction, C_H/C_{Ho}, which is a reasonable approximation for the analytical expression given by Marxman[19] for a wide B_g range of 0-14.

$$\frac{C_H}{C_{Ho}} = \frac{C_f}{C_{fo}} \cong \frac{2}{2 + 1.25 B_g^{0.75}} =$$

$$= \frac{C_{B1}}{C_{B1} + C_{B2}(\dot{r}_v/\dot{r}_{cl})^{0.75}} \quad (14)$$

Here the coefficients are defined as

$$C_{B1} \equiv \frac{2}{2 + 1.25 B^{0.75}} \quad \text{and} \quad C_{B2} \equiv \frac{1.25 B^{0.75}}{2 + 1.25 B^{0.75}}. \quad (15)$$

Note that for the purposes of this study for which the accuracy at low B values is essential, it is not acceptable to adapt one of the forms that are commonly used in the hybrid literature[1] (i.e. $C_H/C_{Ho} = B^{-0.68}$). These exponential expressions predict unrealistically large blocking factors (even larger than one) for B values close to zero. Also note that B is the classical blowing parameter and $\dot{r}_{cl}$ is the classical regression rate of the system in the case of no entrainment. Following Marxman[1], the classical regression rate can be written as

$$\dot{r}_{cl} = \frac{0.03 \mu_g^{0.2}}{\rho_s}\left(1 + \dot{Q}_r/\dot{Q}_c\right)B \; C_{B1}G^{0.8}z^{-0.2}. \quad (16)$$

Based on the arguments in the proceeding section (i.e. Eq. 9) the entrainment regression rate can be expressed in terms of the mass flux in the port and the total regression rate.

$$\dot{r}_{ent} = a_{ent}\frac{G^{2\alpha}}{\dot{r}^{\beta}} \quad (17)$$

where the entrainment coefficient is introduced as

$$a_{ent} = K\frac{C_f a_t^{\beta} \rho_l}{\mu_l \rho_s}. \quad (18)$$

Here we have ignored the dependence of the thickness coefficient on the vaporization regression rate as suggested by Eq. 12. This is an excellent assumption for the case of large radiative absorptivity in the liquid phase and a reasonable approximation for the other extreme of very small absorptivity, since the regression rate only appears inside the natural logarithm. Note that the entrainment coefficient, a_{ent}, is primarily a function of the properties of the selected propellant.

Eqs. 10, 11, 12, 13, 17 and 18 together with the blowing correction expression, Eq. 14, form a

nonlinear set of algebraic equations which can be solved for a given propellant combination to obtain the total regression rate as a function of the axial location and local mass flux.

It is convenient to cast the regression rate equations given in the preceding paragraphs in the nonlinear form by introducing the following variables that are normalized by the classical regression rate.

$$\phi = \frac{\dot{r}}{\dot{r}_{cl}}, \; \phi_v = \frac{\dot{r}_v}{\dot{r}_{cl}}, \; \phi_{ent} = \frac{\dot{r}_{ent}}{\dot{r}_{cl}}$$

$$\text{and } R_{ent} = a_{ent} \frac{G^{2\alpha}}{\dot{r}_{cl}^{\beta+1}}$$

The set of nonlinear equations for the three unknown non-dimensional regression rates become.

$$\phi = \phi_v + \phi_{ent} \tag{19a}$$

$$\phi_v + \left(R_{he} + R_{hv} \frac{\phi_v}{\phi} \right) \phi_{ent} = \frac{Fr}{C_{B1} + C_{B2}\phi_v} \tag{19b}$$

$$\phi_{ent} = \frac{R_{ent}}{\phi^\beta} \tag{19c}$$

For the purposes of this paper, we will ignore the effect of surface roughness on the regression rate and assume *Fr=1* and we will use a thickness exponent of 2 as suggested by the Gater and L'Ecuyer scaling law for the entrainment mass transfer. For a selected value of the entrainment parameter, R_{ent}, the nonlinear algebraic Eqs. 19a, 19b and 19c can be solved numerically to determine the three unknown non-dimensional regression rates. For the range of entrainment parameters 0-300, solutions have been produced for the case of *B=4.7*, $R_{he} = 0.051$ and

$R_{hv} = 0.433$. The results are plotted in Figure 2. As shown in the figure, the entrainment component of the regression rate increases rapidly with growing entrainment parameter. The increase in the non-dimensional entrainment regression slows down as R_{ent} increases. The total regression rate follows a very similar trend, whereas the vaporization regression rate decreases slowly from its value of 1 at $R_{ent} = 0$. At large values of the entrainment parameter, the entrainment component of the regression rate dominates the vaporization. Note that the total regression rate asymptotes to the value of $\phi = 1/R_{he}C_{B1}$. It has been determined that the following simple equation fits the predicted total non-dimensional regression rate in the range of $0 < R_{ent} < 300$, which covers the practical range of operation.

$$\phi = 1 + 0.61 R_{ent}^{0.40} \tag{20}$$

Even though the curve fit expression given by Eq. 20 is calculated for the numerical values of *B=4.7*, $R_{he} = 0.051$ and $R_{hv} = 0.433$, it has been determined that the variation in the total regression rate with the *B*, R_{he} or R_{hv} is small. Thus Eq. 20 can be treated as a universal regression rate expression for the thickness exponent of 2 (for Gater and L'Ecuyer scaling law). For other values of the thickness exponent, β, curve fit expression with the same form but with different coefficient and exponent should be used.

For predicting the regression rate behavior of a class of liquefying fuels, it is critical to understand the functional dependence of the entrainment parameter on the inherent properties of the fuel. From Eqs. 6, 9 and 16, one can write the following expression for the entrainment parameter.

$$R_{ent} = K \frac{a_t^\beta \rho_s^\beta \rho_l}{\mu_l} C_{B1}^{-\beta} B^{-(\beta+1)} \left(1 + \dot{Q}_r/\dot{Q}_c\right)^{-(\beta+1)} G^{2\alpha-0.8\beta-1} z^{0.2\beta} \tag{21}$$

Note that we have ignored the effect of the two phase flow on the skin friction coefficient, namely

$$C_f = \frac{C_f}{C_{fo}} C_{fo} \cong C_{B1} C_{fo} = 0.03 \left(\frac{G\,z}{\mu_g} \right)^{-0.2} C_{B1}. \tag{22}$$

This is a fairly good assumption since the variation of the non-dimensional vaporization regression rate is relatively small for practical systems (i.e. see Figure 2).

The constant, 0.03, and the gas viscosity, μ_g, have been incorporated into the constant entrainment parameter constant, *K*. For $\alpha = 1.5$ and $\beta = 2$ Eq. 21 takes the following form

9
American Institute of Aeronautics and Astronautics

$$R_{ent} = K \frac{a_t^2 \rho_s^2 \rho_l}{\mu_l} C_{B1}^{-2} B^{-3} \left(1 + \dot{Q}_r / \dot{Q}_c\right)^{-3} G^{0.4} z^{0.4} \ .(23)$$

Note that R_{ent} is a strong function of the material properties and a weak function of the local mass flux and the axial location.

The form of the equation for the classical regression rate hints that the fuel solid density and the blowing parameter are the only variables that strongly depend on the properties of the particular fuel being used. Even though the solid density can easily be measured or estimated for a given fuel, the blowing parameter is difficult to predict. Also note that the entrainment regression rate calculation using Eqs. 19a, 19b and 19c requires the knowledge of the blowing parameter. For the purposes of this paper, the blowing parameter will be roughly estimated with use of the following formula derived by Marxman *et al*[1]

$$B = \frac{1 + \left[1 + (O/F)_f\right]\Delta h / h_v}{(O/F)_f} \ . \tag{24}$$

Here $(O/F)_f$ is the oxidizer to fuel ratio of the hybrid diffusion flame, $\Delta h = h_b - h_s$ is the enthalpy difference between the flame and the surface and h_v is the effective heat of gasification. We will assume that the flame oxidizer to fuel ratio and the enthalpy at the flame are constant for the entire series of n-alkanes and the numerical values of $(O/F)_f = 2$ and $h_v = 2,652 \ cal / g$ will be used in the calculations. The surface enthalpy and the effective heat of gasification will be calculated for each case. It has been determined that the effect of moderate variations in the assumed flame oxidizer to fuel ratio on the total regression rate is fairly small.

For convenience we will define the classical regression rate of the infinitely long chain HDPE polymer as the reference classical regression rate, $(\dot{r}_{cl})_{ref}$. Based on this definition and using Eq. 16, the classical regression rate for an arbitrary carbon number *n* can be written as

$$\phi_{cl} = \frac{\dot{r}_{cl}}{(\dot{r}_{cl})_{ref}} = \frac{(\rho_s)_{ref}}{\rho_s} \frac{B \ C_{B1}}{(B \ C_{B1})_{ref}} \ . \tag{25}$$

Here we have assumed that the radiative to convective heat flux ratio is constant for the entire series of normal alkanes. Based on Eq. 25, the total regression rate can

be expressed in terms of the regression rate of the HDPE polymer.

$$\dot{r} = \phi_{cl}\phi \ (\dot{r}_{cl})_{ref} \tag{26}$$

Note that the entrainment parameter constant *K* is the only unknown variable introduced in the liquid layer combustion theory, which needs to be evaluated by matching the measured regression rate for a selected carbon number to the regression rate predicted by the theory. Note that this a single point matching and can only be used to adjust the level of the regression rate-carbon number curve. The shape of the regression rate curve (or regression rates for all other carbon numbers) is uniquely determined by the theory.

4. Material Properties for n-Alkanes:

The calculation of the regression rate for the entire homologous series of normal alkanes requires the knowledge of the fuel properties over a wide range of temperatures and carbon numbers. In this section we will discuss some of the material property estimation techniques as given in the chemistry literature: initially for pure n-alkanes (i.e. materials composed of one carbon number) and later for mixtures of n-alkanes.

4.1. Pure n-Alkanes: A reasonably accurate method of estimating the thermophysical properties of homologous series has been reported by Marano and Holder in Ref. 20, 21 and 22. They have established a class of equations which are referred to as asymptotic behavior correlations (or ABCs) that are used to predict the properties of homologous series accurately especially for the moderate to high molecular weight elements of the series.

Here we discuss only a few of the important properties that are estimated to evaluate the regression rate.

Critical Properties: The critical temperature and pressure for the homologous series of n-alkanes are predicted by the ABC method and plotted in Figures 3 and 14. The important observation is that the critical pressure drops with increasing carbon number. In fact for infinite carbon number the critical pressure asymptotes to zero as predicted by many of the state equations for long chain molecules. This implies that most hybrid systems using paraffin based fuels are operating in the supercritical regime for which the distinction between the liquid and vapor phases disappear. This important operating regime will be discussed in detail in section 5.3 of this paper. The critical temperature increases monotonically with increasing molecular weight and asymptotes to the value of 1020.7 K as the carbon number approaches infinity.

10

Viscosity: It will be shown later in this paper that the melt layer viscosity is one of the most important parameters that establish the regression rate of a liquefying hybrid propellant. The prediction of viscosity is a difficult process. Multiple estimation methods need to be used to establish a reasonably accurate depiction of the viscosity behavior over the entire range of carbon numbers. We start with the ABC method for which the viscosity can be calculated as using the following set of equations.

$$Y = Y_{\infty,0} + \Delta Y_\infty (n - n_o) - \Delta Y_o \exp\left[-\beta(n-n_o)^\gamma\right] \quad (27)$$

$$\Delta Y_o = A_o + B_o/T + C_o \ln T + D_o T^2 + E_o/T^2 \quad (28b)$$

$$\Delta Y_\infty = A_\infty + B_\infty/T + C_\infty \ln T + D_\infty T^2 + E_\infty/T^2 \quad (28b)$$

and

$$\mu_l = \exp(Y). \quad (29)$$

It has been reported that the following coefficients fit n-alkane data the best[22].

$$n_o = -2.293981, \; Y_{\infty,0} = 57.8516$$
$$\beta = 2.476409, \; \gamma = 0.0112117$$

The coefficients of temperature dependent terms given by Eqs. 28a and 28b, are presented in Table 1. Note that the data used in the fit process was in the range of 0-300 C.

It turns out that the ABC method prediction for the viscosity is inaccurate for compounds with carbon numbers less than 11. For light members of the series we have used the temperature dependent viscosity data as discussed in Ref 23. Reference 23 reports a best curve fit to the measured viscosity data in a wide range of temperatures for each n-alkane and is expected to be fairly accurate when evaluated within the suggested temperature range.

Unlike the other thermophysical and transport properties, the accuracy of the viscosity prediction by the ABC method reduces with increasing molecular weight for carbon numbers larger than approximately 70. The anomalous behavior of viscosity is due to the complex rheology of liquids made out of long chain molecules. For that reason, another method for estimating the zero shear viscosity of heavier molecules (i.e. polymers), which was reported by Bicerano[24], has been implemented. This method can be used to evaluate the viscosity of liquids composed of large n-alkane molecules at a specified temperature, *T*. The estimation process is outlined in the following paragraphs.

First the critical molecular weight (in *g/mole*) can be estimated using the relation

$$M_{cr} = 169\left(\frac{M_m}{K_{cr}}\right)^4 \quad (30)$$

where the constant K_{cr} is 13.10 and the molecular weight of the monome*r*, M_m, is 28.05 g/mole for the case of n-alkanes.

The glass transition viscosity and the critical viscosity can be calculated using the following relations.

$$\mu_{Tg} = 10^{E_v\left(0.052 - 8.5 \; 10^{-5} T_g\right)/T_g - 1.4} \quad (31a)$$

$$\mu_{cr} = \mu_{Tg} 10^{(T_g - T)E_v/(2.3 R_u T_g T)} \quad (31b)$$

Note that T_g is the glass transition temperature (190 K for polyethylene) and R_u is the universal gas constant. The activation energy for viscous flow is defined as

$$E_v = \left(\frac{H_{tot}}{M_m}\right)^3 \quad (32a)$$

where

$$H_{tot} = H_{add} + 250 \; N_{side}. \quad (32b)$$

The numerical value of H_{add} is estimated to be 840 $kJ^{1/3} g \; mol^{2/3}$ for polyethylene and the number side chains, N_{side}, is assumed to be zero (linear polyethylene molecule).

The zero shear viscosity of a compound with the molecular weight M_w can be estimated using the following relations:

$$\mu = \mu_{cr} \frac{M_w}{M_{cr}} \quad \text{for } M_w \leq M_{cr} \quad (33a)$$

$$\mu = \mu_{cr}\left(\frac{M_w}{M_{cr}}\right)^{3.4} \quad \text{for } M_w > M_{cr} \quad (33b)$$

For n-alkanes, the Bicerano method predicts a critical molecular weight (entanglement molecular weight) of 3,552.5 g/mol which corresponds to a carbon number of 254. For the homologous series of n-alkanes the

viscosity behavior with increasing carbon number changes dramatically at this carbon number. The reason for the change in character is due to the extra restrictions on the molecular motion induced by the entanglement of long molecules. The rate of viscosity increase with carbon number decreases above the entanglement molecular weight. Also the Newtonian behavior of the low carbon number n-alkanes becomes invalid (shear thinning phenomenon take place). Please note that the molecular entanglement behavior has also been observed in long chain molecules other than n-alkanes.

Liquid Density: The liquid density is another variable that directly influences the entrainment character of a liquefying hybrid fuel. The densities of normal alkanes with carbon numbers less than 11 will be estimated using the temperature dependent density data reported in Ref. 23. For carbon numbers larger than 11 the ABC method predictions are accurate.

$$Y = Y_{\infty,0} + \Delta Y_{\infty}(n + n_o) - \Delta Y_o \exp\left[-\beta(n + n_o)^{\gamma}\right] \quad (34a)$$

and

$$\rho_l = 1000\frac{M_w}{Y} \quad (34b)$$

The coefficients of temperature dependent terms, Eqs. 28a and 28b, are also presented in Table 1. It has been noted that the following coefficients fit n-alkane data the best.

$$n_o = -1.388524, \; Y_{\infty,0} = 0$$
$$\beta = 5.519846, \; \gamma = 0.0570632$$

Note that unlike the viscosity, the liquid densities can be accurately predicted by the ABC method for all carbon numbers larger than 11.

Other Thermophysical Properties: Most of the other thermophysical properties of the fuel that are needed in the regression rate calculations, such as the thermal conductivity and the heat capacity of the liquid, has been estimated using the ABC method as discussed in Refs. 20, 21 and 22. The solid density, solid heat capacity and heat of melting are not considered in Refs. 20, 21 and 22. Using data reported in other literature[23], we have developed our own asymptotic relations to predict these quantities. For example, the molar heat of melting can be approximated by the following linear function of *n*.

$$\hat{L}_m = 0.601(n - 1.536) \; kcal/mole. \quad (35)$$

4.2. Mixtures of n-Alkanes: Most practical paraffinic fuel systems are not composed of a single type of n-alkane molecule, instead they are mixtures of straight chain molecules. The paraffinic systems form an extensive class of fuels with well known members such as kerosene (a liquid under standard conditions), paraffin waxes, PE waxes and HDPE polymer. The estimation of the material properties for the mixtures of alkanes is a complex process[25]. A rigorous treatment requires the knowledge of the details of the molecular weight distribution which is not readily available for most materials. Furthermore the mixing rules are complex and require the evaluation of a number of empirical parameters. In this paper, we will bypass these difficulties by evaluating all necessary material properties other than viscosity at the number averaged carbon number. For an accurate estimation, the viscosity of mixtures will be calculated using the weight averaged carbon number. A justification for this approach is given Ref. 24.

At this point we will introduce a useful concept commonly used in polymer science, polydispersity (*PD*), which is defined as the ratio of the weight averaged carbon number to the number averaged carbon number. In general terms, the polydispersity characterizes the broadness of the molecular weight distribution in a mixture. For example for a monodisperse mixture *PD* is one and its value increases as the distribution gets broader.

In this simplified approach, two quantities are adequate to describe a paraffinic mixture, namely the number averaged carbon number, *n*, and the polydsipersity, *PD*. Note that viscosity should be evaluated at *n*PD* and all other properties will be calculated using *n*.

In Figure 4, the viscosity as a function of the weight averaged carbon number has been plotted for four temperatures 90, 120, 140 and 190 C. Note that each plot is constructed using the three prediction methods outlined in the previous paragraphs within their acceptable range of carbon numbers. Data points for the paraffin wax FR5560, and the PE wax Marcus 200 have also been included for comparison purposes. The paraffin data has been measured by the authors using a Grace Instruments viscometer. The melting point for this particular grade of wax is 70 C, suggesting a number averaged carbon number of approximately 32. A polydispersity of approximately 1.1 has been estimated by matching the measured viscosity to the ABC method prediction. The viscosity information for the PE wax has been supplied by the vendor, Marcus Oil and Chemical Company. The number averaged and weight averaged carbon numbers for this particular PE wax grade has been reported to be 79 and 134, respectively, yielding a polydispersity of 1.71. Note

that the viscosity prediction for the paraffin wax and for the PE wax at 190 are in good agreement with the experimental data. The viscosity prediction for the PE wax at 121 C and 140 C are high possibly due to measurement errors (both in viscosity and also in the weight averaged molecular weight).

5. Estimation of the Condensed Phase Temperature Field:

Most of the thermophysical properties discussed in the previous section are strong functions of temperature. Thus for an accurate calculation of the regression rate it is critical to evaluate the material properties at a temperature that is representative of the layer for that particular fuel composition. In the following paragraphs we discuss the three key temperatures that need to be identified for each formulation: 1) ambient temperature, 2) melting temperature and 3) surface temperature.

5.1. Ambient Temperature:

Ambient temperature is the bulk temperature of the solid fuel grain. In our calculations, we assume the following temperature variation as a function of the carbon number for the homologous series of n-alkanes.

$$\text{If } T_m < 298 \ K \quad T_a = T_m - 20 \ K \qquad (36a)$$

$$\text{If } T_m \geq 298 \ K \quad T_a = 298 \ K \qquad (36b)$$

Even though the selection of the ambient temperature is somewhat arbitrary, as long as $T_m > T_a$, the aforementioned ambient temperature assignment is a reasonable selection from a practical point of view.

5.2. Melting Temperature:

The melting temperature of the n-alkanes can be estimated based on the ABC method using the following equations.

$$Y = Y_\infty - \left(Y_\infty - Y_o\right)\exp\left[-\beta\left(n - n_o\right)^\gamma\right] \qquad (37)$$

and

$$T_m = Y . \qquad (38)$$

The following coefficients fit n-alkane data the best[21].

$$n_o = 0.34979 , \ Y_o = -6288460$$
$$Y_\infty = 418.07 , \ \beta = 8.929364 , \ \gamma = 0.0690406$$

The measured melting temperatures of n-alkanes[23] along with the predicted values by the ABC method are shown in Figure 5. The odd-even oscillation of melting temperatures at low carbon numbers is common in many homologous series and this cannot be predicted by the ABC method which is accurate for carbon numbers larger than 11. The oscillation of the melting point is due to the different crystal structures of the odd and even carbon numbered n-alkanes as discussed in Ref. 21. For the carbon numbers less than 11, melting point data as shown in Figure 5 has been used instead of the ABC prediction. The data points for the paraffin and PE waxes considered in this study have also been included in the figure.

5.3. Surface Temperature:

As discussed earlier, the accurate determination of the surface temperature is a key step in the development of a comprehensive combustion model for the liquefying propellants. The surface temperature, along with the melting temperature, determines the effective melt layer temperature at which the critical fluid properties, such as viscosity and density, should be evaluated. These key fluid properties influence the stability of the fluid layer and governs the entrainment mass transfer from the high density fluid layer to the gas stream in the port.

The definition and the determination of the surface temperature is a difficult process. The fundamental thermodynamic properties of the fuel material (i.e. critical properties and the state equation) along with the operational parameters of the motor, such as the chamber pressure, dictate the nature of the surface phenomenon. For homologous series, a large variation in the thermodynamic properties with the carbon number is expected. Thus, the combustion modeling of the entire series requires good understanding of various processes that take place at the surface. Specifically, if the partial pressure of the fuel is less than the critical pressure, the evaporation process determines the surface temperature (see Figure 6a for a schematic for this mode of operation). This mode of operation is expected for the light members of the series for which the critical pressure is high, or for moderate carbon numbered members if the chamber pressure is extremely low. If the partial pressure at the surface is larger than the critical pressure, the thermodynamic distinction between the liquid and gas phases is lost and the surface as defined by the physical phase change phenomenon disappears. The surface tension also diminishes and the fluid heats from the melting temperature to the surface temperature, which is now dictated by chemistry, namely the pyrolysis process of the fuel molecules. In this case, the surface temperature is defined as the temperature for which an arbitrarily set amount of fuel is thermally decomposed into smaller molecules (See Figure 6b for a schematic of

this case). Fortunately the activation energies for the pyrolysis processes for most hydrocarbons are large and the variations in the surface fuel mass fraction does not effect the surface temperature significantly.

In the following sections we will derive relations to estimate the surface temperature and the liquid layer thickness for these two distinct operational regimes. Initially the effect of the entrainment on the surface temperature will be ignored. In other words, the surface temperatures estimated using the following procedures are expected to be valid at the onset of the entrainment process, but not during operation with entrainment.

5.3.1. Kinetic Theory Derivation:

As discussed in the previous paragraphs, if the partial pressure of the vapor, P_f, is less than the critical pressure for the fuel, the surface temperature will be determined by an evaporation process. This condition can be written in terms of the chamber pressure as

$$Y_{fs}P_c = P_f < P_{cr} . \qquad (39)$$

In this section, using the concepts of the kinetic theory, we will derive a formula for the surface temperature in terms of the properties of the fuel and the operational parameters of the motor.

The kinetic theory predicts the mass of material evaporating from the liquid surface into the vapor phase as[26]

$$\dot{m}_{evap} = \mu_{mol} n_\sigma \bar{\upsilon} \frac{(\varepsilon/kT_s)^{s-1}}{(s-1)!} e^{-\varepsilon/kT_s} . \qquad (40)$$

Here n_σ is the number density of the molecules on unit surface, $2s$ is the number of quadratic terms among which the activation energy is distributed, $\bar{\upsilon}$ is the oscillation frequency of the molecules in the liquid phase, k is the Boltzmann's constant, ε is the activation energy for evaporation and μ_{mol} is the molecular mass. Note that if the activation energy of condensation is assumed to be zero, ε can be regarded as the heat of vaporization per molecule.

Similarly the mass of the vapor condensing can be written as

$$\dot{m}_{cond} = \frac{P_f \mu_{mol}}{kT_s} \left(\frac{kT_s}{2\pi\mu_{mol}} \right)^{1/2} =$$

$$= P_f \left(\frac{\mu_{mol}}{2\pi kT_s} \right)^{1/2} . \qquad (41)$$

The mass balance at the liquid gas interface requires that

$$\dot{m}_v = \rho_l \dot{r}_v = \dot{m}_{evap} - \dot{m}_{cond} = \mu_{mol} n_\sigma \bar{\upsilon} \frac{(\varepsilon/kT_s)^{s-1}}{(s-1)!} e^{-\varepsilon/kT_s} - P_f \left(\frac{\mu_{mol}}{2\pi kT_s} \right)^{1/2} . \qquad (42)$$

For the equilibrium case of $\dot{r}_v = 0$, Eqs. 40, 41 and 42 can be combined to yield the Clausius-Clapeyron equation for the vapor pressure.

$$P_f = \left(2\pi M_w R_u\right)^{1/2} \frac{n_\sigma \bar{\upsilon}}{(s-1)!} \left(\frac{\hat{L}_v}{R_u} \right)^{s-1} \frac{1}{T_s^{s-3/2}} e^{-\hat{L}_v/R_u T_s} = A_{cc} \frac{1}{T_s^{s-3/2}} e^{-\hat{L}_v/R_u T_s} \qquad (43)$$

Note that the heat of vaporization, $\hat{L}_v$, the universal gas constant and molar masse M_w are defined in terms of the Avogadro's number, N_a, as follows.

$$\hat{L}_v = \varepsilon \ N_a , \ R_u = k \ N_a \text{ and } M_w = \mu_{mol} N_a .$$

At the normal boiling point $T_s = T_b$ and $P_f = P_a = 1 \ atm$, this equation can be used to evaluate the constant, A_{cc}.

$$A_{CC} = \left(2\pi M_w R_u\right)^{1/2} \frac{n_\sigma \bar{\upsilon}}{(s-1)!} \left(\frac{\hat{L}_v}{R_u} \right)^{s-1} =$$

$$= P_a T_b^{s-3/2} e^{\hat{L}_v/R_u T_b} \qquad (44)$$

Now Eqs. 42 and 44 can be combined to yield the following non-dimensional relation between the regression rate, partial pressure and the surface temperature.

$$
\frac{\dot{r}_v \rho_l}{P_a}\left(\frac{2\pi R_u T_b}{M_w}\right)^{1/2} =
$$

$$
\left(\frac{T_b}{T_s}\right)^{s-1} e^{-\left(\hat{L}_v/R_u T_b\right)\left(T_b/T_s - 1\right)} - \frac{P_f}{P_a}\left(\frac{T_b}{T_s}\right)^{1/2} \quad (45)
$$

For a given material, regression rate and vapor partial pressure, the temperature ratio T_b/T_s can be solved from this non-dimensional algebraic equation. Note that normal boiling temperature T_b is a known quantity for a given material and the pressure P_a is *1 atm* by definition.

The variation of the internal degrees of freedom, s, with the carbon number and the temperature at which the heat of vaporization would be evaluated still need to be determined in order to estimate the surface temperature. For the homologous series of normal alkanes we have decided to use the heat of vaporization at the normal boiling temperature, $\hat{L}_v = \hat{L}_{v,T_b}$ (since it is readily available) and the following simple variation for s with the carbon number n, $s = n^{\alpha_s}$. The normal boiling temperature and the heat of vaporization at the normal boiling temperature for the series of n-alkanes has been evaluated using the ABC method[20, 21, 22].

The best value of α_s is determined by matching the vapor pressure predicted by Eq. 45 (for the case of zero regression rate) to the vapor pressure predicted by the ABC method and the experimental data given in the literature[23]. It has been determined that, in the carbon number range of 5-20, the best fit to the ABC prediction can be obtained for $\alpha_s = 0$ (i.e. $s = 1$) which simplifies Eq. 45 to

$$
\frac{\dot{r}_v \rho_l}{P_a}\left(\frac{2\pi R_u T_b}{M_w}\right)^{1/2} =
$$

$$
= e^{-\left(\hat{L}_{v,T_b}/R_u T_b\right)\left(T_b/T_s - 1\right)} - \frac{P_f}{P_a}\left(\frac{T_b}{T_s}\right)^{1/2} . \quad (46)
$$

For larger carbon numbers the prediction by Eq. 46 and the ABC method have deviated progressively with increasing carbon number. Part of the discrepancy is due to the high error in the ABC method predictions for the larger carbon numbers. In fact, Eq. 46 resulted in a better match at the critical point compared to the ABC method estimate.

Figure 7 shows the vapor pressure temperature variation for four n-alkanes with carbon numbers 5, 10, 15 and 20 as predicted by Eq. 46. The critical points for these alkanes are also shown in the figure. Note that the part of the plots beyond the critical temperature does not have any physical meaning and should be ignored. Also note that the match between the vapor line and the critical point is fairly good especially for low carbon numbers. The accuracy of the surface temperature prediction for carbon numbers larger than 20 is not significant since the fuel systems with high carbon numbers would operate in the supercritical regime for which the surface temperature is not determined by the evaporation process.

It can be shown that, for typical conditions encountered in hybrid rockets, the regression rate term that appears on the left hand side of Eq. 46, is several orders of magnitude smaller than the terms that are on the right hand side. Thus for liquefying hybrid fuels operating in the subcritical regime, quasi-phase equilibrium is a valid assumption.

The partial pressure of the fuel is not a variable that can be easily measured. Thus it needs to be related to variables that are measurable such as the chamber pressure. Here we follow the approximations introduced by Marxman[1] in his diffusion limited model for the combustion of classical hybrid rockets. The Reynolds analogy between the flame zone and the surface yields

$$
\frac{h_b - h_s}{h_v} = \frac{\Delta h}{h_v} = \frac{Y_{fb} - Y_{fs}}{Y_{fs} - 1} . \quad (47)
$$

Here h_b is the enthalpy of the gas at the flame, h_s is the enthalpy of the gas at the surface, h_v is the effective heat of vaporization, Y_{fs} is the fuel mass fraction at the surface and Y_{fb} is the fuel mass fraction at the flame. Based on the flame sheet approximation, the fuel mass fraction at the flame can be assumed to be zero. Under this condition, Eq. 47 can be used to solve for the fuel mass fraction at the surface.

$$
Y_{fs} = \frac{\Delta h/h_v}{\Delta h/h_v + 1} \quad (48)
$$

The partial pressure of the fuel at the surface can now be written in terms of the chamber pressure P_c and the enthalpy ratio $\Delta h/h_v$ as

$$
P_f = Y_{fs} P_c = \frac{\Delta h/h_v}{\Delta h/h_v + 1} P_c . \quad (49)
$$

Note that the mass fraction of the fuel at the surface increases as the enthalpy ratio increases. For typical conditions encountered in hybrid rockets, the surface mass fraction is expected to be in the range of 0.75-0.90.

In the subcritical case, the melt layer thickness expressions given in section 3 of this paper can be used with no modifications.

5.3.2. Supercritical Case - Thermal Analysis:

In this section we assume that the conditions for supercritical operation exist and the relevant surface phenomenon is governed by the pyrolysis chemistry. A thermal analysis which takes into account the chemical reactions will be conducted to determine the surface temperature and the thickness of the melt layer.

In our model, the solid-liquid fuel slab has been divided into three zones: 1) Pyrolysis zone, 2) Liquid zone and 3) Solid zone. A schematic for the model is shown in Figure 6b. In the following paragraphs the field equations for each zone will be derived. For the sake of simplicity, the material properties will be assumed to be constant within the liquid and solid zones. Furthermore, the properties in the pyrolysis zone are taken equal to the properties in the liquid zone.

1) Pyrolysis Zone: This is a thin layer next to the surface (for large activation energies) in which the pyrolysis reactions take place. In this zone the temperature varies from T_p for which the pyrolysis reactions start to the surface temperature T_s. The mass fraction of the fuel reduces from one to a low value due to thermal cracking of the original n-alkane molecules forming the fuel bulk. The surface temperature is defined based on an arbitrarily selected value for the n-alkane mass fraction at the surface. This condition also constitutes a definition for the surface.

The energy equation and the equation for the mass fraction of the fuel can be written as

$$\frac{d^2T}{dx_p^2} + \frac{1}{\delta_l}\frac{dT}{dx_p} =$$

$$= \frac{q_p \rho_l a_p}{\lambda_l} e^{-E_a/R_u T} Y_f^k - \frac{\dot{Q}_r a_l}{\lambda_l} e^{-a_l x_p} \quad (50)$$

$$\frac{dY_f}{dt} = -a_p e^{-E_a/R_u T} Y_f^k \quad (51)$$

Using the average liquid velocity[8,9] (i.e. $\dot{r}\rho_s/\rho_l$), the mass fraction equation can be converted from the time base into the displacement base as

$$\frac{dY_f}{dx_p} = -\frac{a_p \rho_l}{\dot{r}\rho_s} e^{-E_a/R_u T} Y_f^k . \quad (52)$$

Eqs. 50 and 52 should be solved simultaneously with the following boundary conditions to obtain the temperature and mass concentration profiles in the reaction zone.

For $x_p = 0$ $T = T_s$ and $Y_f = Y_{fs}$
For $x_p = \delta_p$ $T = T_p$ and $Y_f = 1$

To our knowledge, a closed form solution for this set of nonlinear ordinary differential equations does not exist. However, a solution can be obtained by employing the large activation energy approximation. In order to demonstrate the relative importance of individual terms, Eq. 50 will be normalized using the following non-dimensional variables

$$\theta = \frac{T - T_s}{T_p - T_s} \text{ and } \bar{x}_p = \frac{x_p}{\delta_p} \quad (53)$$

$$\frac{d^2\theta}{d\bar{x}_p^2} + \frac{\delta_p}{\delta_l}\frac{d\theta}{d\bar{x}_p} = \frac{q_p \rho_l a_p \delta_p^2}{\lambda_l(T_p - T_s)} e^{-E_a/R_u[(T_p-T_s)\theta+T_s]} Y_f^k + \frac{h_v}{C_l(T_p - T_s)}\frac{\dot{Q}_r/\dot{Q}_c}{1+\dot{Q}_r/\dot{Q}_c}\frac{\delta_p}{\delta_l}\frac{\delta_p}{\delta_r} e^{-\delta_p \bar{x}_p/\delta_r} \quad (54)$$

For large activation energies the thickness of the radiation zone will be small, namely $\delta_p/\delta_l \ll 1$.

Therefore the convection term is negligible compared to the other terms and will be dropped for the sake of simplicity. The validity of this assumption will be checked later in this section.
The radiative heating term can also be ignored in the following two extremes:

1) Case 1: Very large absorptivity ($\delta_p/\delta_r \gg 1$):
   The exponential term drives the radiative heating in the reaction zone to zero. All the radiation is absorbed at the surface (in a very thin layer compared to the reaction zone)
2) Case 2: Very small absorptivity ($\delta_p/\delta_r \ll 1$): The coefficient drives the

heating in the reaction zone to zero. All radiation is absorbed beneath the radiation zone.

In either case, the field equation for the temperature reduces to

$$\frac{d^2T}{dx_p^2} = \frac{q_p \rho_l a_p}{\lambda_l} e^{-E_a/R_u T} Y_f^k . \tag{55}$$

The set of Eqs. 51 and 55 can now be solved to determine the temperature and mass fraction field in the reaction zone. Note that Eq. 55 can be rearranged as

$$\frac{1}{2}\frac{d}{dx_p}\left(\frac{dT}{dx_p}\right)^2 = A\frac{dT}{dx_p} e^{-E_a/R_u T} Y_f^k . \tag{56}$$

Here we have introduced the following variable for convenience

$$A = \frac{q_p \rho_l a_p}{\lambda_l} . \tag{57}$$

Similarly Eq. 51 can be written as

$$\frac{dY_f}{dT}\frac{dT}{dx_p} = -\frac{a_p \rho_l}{\dot{r}\rho_s} e^{-E_a/R_u T} Y_f^k . \tag{58}$$

Now we define the temperature gradient variable $u \equiv dT/dx_p$ and Eqs. 56 and 58 can be written in terms of this new variable as

$$\frac{1}{2}du^2 = Ae^{-E_a/R_u T} Y_f^k dT \tag{59}$$

and

$$udY_f = -\frac{a_p \rho_l}{\dot{r}\rho_s} e^{-E_a/R_u T} Y_f^k dT . \tag{60}$$

dT can be eliminated from these two equations to yield.

$$du = \frac{A\dot{r}\rho_s}{a_p \rho_l} dY_f . \tag{61}$$

Equation 61 can be directly integrated to yield

$$u = u_s + \frac{A\dot{r}\rho_s}{a_p \rho_l}\left(Y_f - Y_{fs}\right). \tag{62}$$

The boundary condition at the surface requires that

$$\dot{Q}_s = L_v \rho_s \dot{r} - \lambda_l \frac{dT}{dx_p}\bigg|_{x_p=0} = L_v \rho_s \dot{r} - \lambda_l u_s . \tag{63}$$

Note that for the case of large absoptivity $\delta_p/\delta_r \gg 1$, the surface heat flux is a combination of radiation and convective fluxes, $\dot{Q}_s = \dot{Q}_c + \dot{Q}_r$. Whereas for the case of small absorptivity, $\delta_p/\delta_r \ll 1$, the surface flux is only composed of the convection term $\dot{Q}_s = \dot{Q}_c$. In this paper, we will only consider the case of large absorptivity because of its practical importance. Note that the other extreme case can easily be treated by using the arguments of the following paragraphs.

The definition of the effective heat of gasification, $\dot{Q}_s = h_v \rho_s \dot{r}$ and the variable A can be used to obtain the following linear relation between the temperature gradient variable u and the fuel mass fraction in the reaction zone.

$$u = -\dot{r}\left(B_2 - B_1 Y_f\right) \tag{64}$$

where

$$B_1 = \frac{q_p \rho_s}{\lambda_l} \text{ and } B_2 = \frac{\left(h_v - L_v + q_p Y_{fs}\right)\rho_s}{\lambda_l} . \tag{65}$$

Note that this relation is independent of the reaction order, k.

Substitution of Eq. 64 into Eq. 60 results in

$$-\frac{\dot{r}^2 \rho_s}{a_p \rho_l}\frac{\left(B_2 - B_1 Y_f\right)dY_f}{Y_f^k} = e^{-E_a/R_u T} dT \tag{66}$$

which can be integrated to yield

$$\frac{\dot{r}^2 \rho_s}{a_p \rho_l}\left[\frac{B_2}{1-k}\left(1 - Y_{fs}^{1-k}\right) - \frac{B_1}{2-k}\left(1 - Y_{fs}^{2-k}\right)\right] =$$

$$= I_p = \int_{T_p}^{T_s} e^{-E_a/R_u T} dT . \tag{67}$$

The exponential integral can be approximated using the following arguments. The integrant can be written in terms of a new variable $\zeta = T_s - T$ as

$$\frac{E_a}{R_u T} = \frac{E_a}{R_u (T_s - \zeta)} \cong \frac{E_a}{R_u T_s}\left(1 + \frac{\zeta}{T_s}\right). \qquad (68)$$

Here we have used the Taylor series expansion assuming $\zeta/T_s << 1$. Following this approximation, the integral I_p simplifies to

$$I_p = \int_{T_p}^{T_s} e^{-E_a/R_u T} dT \cong$$

$$\cong \frac{R_u T_s^2}{E_a} e^{-E_a/R_u T_s}\left(1 - e^{-E_a(T_s - T_p)/R_u T_s}\right). \quad (69)$$

Eqs. 67 and 69 and can now be combined to relate the regression rate to the surface temperature

$$\dot{r} = \left\{\frac{R_u T_s^2}{E_a}\frac{a_p \rho_l\left[1 - e^{-E_a(T_s - T_p)/R_u T_s^2}\right]}{\rho_s\left[\frac{B_2}{1-k}\left(1 - Y_{fs}^{1-k}\right) - \frac{B_1}{2-k}\left(1 - Y_{fs}^{2-k}\right)\right]}\right\}^{\frac{1}{2}} e^{-E_a/2R_u T_s} \qquad (70)$$

For the special case of zeroth order reaction, $k=0$, Eq. 70 simplifies to

$$\dot{r} = \left\{\frac{R_u T_s^2}{E_a}\frac{a_p \rho_l\left[1 - e^{-E_a(T_s - T_p)/R_u T_s^2}\right]}{\rho_s(1 - Y_{fs})\left[B_2 - \frac{B_1(1 + Y_{fs})}{2}\right]}\right\}^{\frac{1}{2}} e^{-E_a/2R_u T_s}. \qquad (71)$$

And for a first order reaction, $k=1$, the regression rate expression becomes

$$\dot{r} = \left\{\frac{R_u T_s^2}{E_a}\frac{a_p \rho_l\left[1 - e^{-E_a(T_s - T_p)/R_u T_s^2}\right]}{\rho_s\left[B_2 \ln(\frac{1}{Y_{fs}}) - B_1(1 - Y_{fs})\right]}\right\}^{\frac{1}{2}} e^{-E_a/2R_u T_s}. \qquad (72)$$

Eq. 72 which is derived for the first order reaction case has been used to plot the regression rate as a function of the inverse surface temperature for $C_{32}H_{66}$ at three different fuel mass fraction values at the surface (See Figure 8). The rate constant for this molecule has been calculated by Eq. 98b of section 6. The activation energy and the chamber pressure are assumed to be, 45 kcal/mole and 25 atm, respectively. Figure 8 shows that for a given regression rate, the surface temperature increases slightly with decreasing fuel mass fraction at the surface.

For the special case of no liquid layer (for fuels burning without forming a liquid layer), Eqs. 71 and 72 reduces to the regression rate surface temperature relationship given in Ref. 27.

Thickness of the Pyrolysis Layer: The thickness of the pyrolysis layer can also be estimated using the formalism of the previous paragraphs. Upon the substitution of the linear relation between the temperature gradient and the mass fraction into the energy equation, Eq. 59, one obtains

$$\frac{u du}{(B_2 \dot{r} + u)^k} = \frac{A}{(B_1 \dot{r})^k} e^{-E_a/R_u T} dT . \qquad (73)$$

Integration of this ordinary differential equation results in the following expression

$$\frac{1}{2-k}\left(v_o^{2-k} - v^{2-k}\right) - \frac{B_2 \dot{r}}{1-k}\left(v_o^{1-k} - v^{1-k}\right) = \frac{A}{(B_1 \dot{r})^k}\int_T^{T_s} e^{-E_a/R_u T} dT = \frac{A}{(B_1 \dot{r})^k} I \qquad (74)$$

where

$$v = B_2 \dot{r} + u, \; v_o = B_2 \dot{r} + u_o \; \text{ and } \; I = \int_T^{T_s} e^{-E_a/R_u T}\, dT \,. \tag{75}$$

Note that integral I can be simplified to the following expression

$$I = \int_T^{T_s} e^{-E_a/R_u T}\, dT \cong$$

$$\cong \frac{R_u T_s^2}{E_a} e^{-E_a/R_u T_s}\left(1 - e^{-E_a \zeta/R_u T_s}\right). \tag{76}$$

The thickness can be obtained by integrating the temperature gradient variable, u, from $x_p = 0$ to $x_p = \delta_p$.

$$u = \frac{dT}{dx_p} = -\frac{d\zeta}{dx_p} \tag{77}$$

For sake of simplicity, we will perform the derivation of the reaction layer thickness expression only for the special case of zeroth order reaction, $k=0$ for which Eq. 74 simplifies to

$$u = -B_2 \dot{r}\sqrt{\alpha_1 - \alpha_2 e^{-E_a \zeta/R_u T_s^2}} \tag{78}$$

where

$$\alpha_1 = \left(1 - \frac{\rho_s}{\rho_l}\right) + 2\frac{\rho_s}{\rho_l}\frac{B_2}{B_1} \quad \alpha_2 = -\frac{\rho_s}{\rho_l}\left(2\frac{B_2}{B_1} - 1\right). \tag{79}$$

Combining Eqs. 77 and 78 yields

$$dx_p = \frac{d\zeta}{B_2 \dot{r}\sqrt{\alpha_1 - \alpha_2 e^{-E_a \zeta/R_u T_s^2}}} . \tag{80}$$

Integration of this equation results in the following relation for the thickness

$$\delta_p = \frac{R_u T_s^2}{E_a B_2 \dot{r}} \frac{1}{\sqrt{\alpha_1}}\left\{\ln\left[\frac{1 - \sqrt{\alpha_1}}{1 + \sqrt{\alpha_1}}\right] - \ln\left[\frac{\sqrt{\alpha_1 + \alpha_2 e^{-E_a \zeta_p/R_u T_s^2}} - \sqrt{\alpha_1}}{\sqrt{\alpha_1 + \alpha_2 e^{-E_a \zeta_p/R_u T_s^2}} + \sqrt{\alpha_1}}\right]\right\}. \tag{81}$$

Note that the characteristic thermal thickness in the liquid layer can be written as

$$\delta_l = \frac{\kappa_l}{\dot{r}}\frac{\rho_l}{\rho_s} = \frac{1}{B_3 \dot{r}} \; \text{ where } \; B_3 = \frac{C_l \rho_s}{\lambda_l}. \tag{82}$$

Based on Eqs. 81 and 82, the ratio of the reaction thickness to the liquid layer characteristic thickness can be constructed as

$$\frac{\delta_p}{\delta_l} = \frac{R_u T_s}{E_a}\frac{B_3 T_s}{B_2}\frac{1}{\sqrt{\alpha_1}}\left\{\ln\left[\frac{1 - \sqrt{\alpha_1}}{1 + \sqrt{\alpha_1}}\right] - \ln\left[\frac{\sqrt{\alpha_1 + \alpha_2 e^{-E_a \zeta_p/R_u T_s^2}} - \sqrt{\alpha_1}}{\sqrt{\alpha_1 + \alpha_2 e^{-E_a \zeta_p/R_u T_s^2}} + \sqrt{\alpha_1}}\right]\right\}. \tag{83}$$

Note that the relative thickness of the reaction zone reduces with increasing activation energy. For large activation energies the thickness of the reaction zone is expected to be small and the simplified version of the energy equation should be valid.

Figure 9 shows the variation of the thickness ratio, δ_p/δ_l, as predicted by Eq. 83 as a function of the activation energy for various values of the temperature difference in the reaction layer, $T_s - T_p$. The following values have been used in the construction of the plot:

$$B_1 = 1.43 \ 10^{10}, \ B_2 = 3.08 \ 10^{10}$$

$$B_3 = 2.31 \ 10^7, \ T_s = 962 \ K$$

Figure 9 indicates that the thickness ratio decreases with increasing activation energy and decreasing temperature difference. Moreover for conditions expected in hybrid rocket applications, δ_p / δ_l is likely to be less than 0.05.

In the following paragraphs we will summarize the calculations in the liquid and solid zones in order to derive an expression for the liquid layer thickness.

2) Liquid Zone: In the liquid zone there are no reactions. In the special case of large radiative absorbtivity, the energy equation simplifies to

$$\frac{d^2 T}{dx_l^2} + \frac{1}{\delta_l} \frac{dT}{dx_l} = 0 \ . \tag{84}$$

Boundary conditions

For $x_l = 0 \quad T = T_p$

For $x_p = h \quad T = T_m$

Eq. 84 can be directly integrated to yield

$$T(x_l) = T_p + \frac{T_p - T_m}{\delta_l (e^{-h/\delta_l} - 1)} \left(1 - e^{-x_l/\delta_l}\right) \tag{85}$$

3) Solid Zone: In the solid zone there are also no reactions. In the special case of large radiative absorbtivity, the energy equation becomes

$$\frac{d^2 T}{dx_s^2} + \frac{1}{\delta_s} \frac{dT}{dx_s} = 0 \ . \tag{86}$$

Note that the following boundary conditions must hold

For $x_s = 0 \quad T = T_m$

For $x_s \to \infty \quad T = T_a$

Eq. 86 can be integrated to obtain

$$T(x_s) = T_s + (T_m - T_a) \ e^{-x_s/\delta_s} \ . \tag{87}$$

Note that the following boundary conditions must also be satisfied:

Zone I-Zone II Boundary:

$$\lambda_l \left. \frac{dT}{dx_p} \right|^I_{x_p = \delta_p} = \lambda_l \left. \frac{dT}{dx_l} \right|^{II}_{x_l = 0} \tag{88}$$

Note that

$$\left. \frac{dT}{dx_p} \right|^I_{x_p = \delta_p} = u \big|_{x_p = \delta_p} = -\dot{r}(B_2 - B_1) = \frac{\dot{r} \rho_s}{\lambda_l} \left[h_v - L_v - q_p \left(1 - Y_{fs}\right) \right] \ . \tag{89}$$

Zone II-Zone III Boundary:

$$\lambda_s \left. \frac{dT}{dx_s} \right|^{III}_{x_s = 0} - \lambda_l \left. \frac{dT}{dx_l} \right|^{II}_{x_l = h} - L_m \rho_s \dot{r} = 0 \tag{90}$$

Upon substitution of the derivative terms in Eq. 89, the following relation for the liquid layer thickness can be obtained.

$$h = \delta_l \ln \left[\frac{h_v - L_v - q_p \left(1 - Y_{fs}\right)}{C_s (T_m - T_a) + L_m} \right] \ . \tag{91}$$

Also note that the following formula for the effective heat of gasification can be derived from the boundary conditions.

$$h_v = C_l (T_s - T_m) + C_s (T_m - T_a) + \\ + L_v + L_m + q_p \left(1 - Y_{fs}\right) \tag{92}$$

Combining Eqs. 91 and 92 results in the simple relation for the melt layer thickness.

$$h = \delta_l \ln \left[1 + \frac{C_l (T_s - T_m)}{C_s (T_m - T_a) + L_m} \right] \tag{93}$$

Note that this expression is same as Eq. 4 which is derived based on the evaporation process at the surface. It has also been shown that the thickness formula for

20

the case of small absorptivity in the supercritical operating regime is exactly the same as the thickness expression in the subcritical regime as given by Eq. 5 of section 3. The derivation has been omitted from this paper for the sake of brevity.

Effect of Entrainment: Note that the surface temperature and thickness expressions derived in the previous sections are only valid without the existence of the entrainment mass transfer. It is clear that the general effect of entrainment will be to reduce the surface temperature. However developing a quantitative model to predict the surface temperature with entrainment is a difficult and highly speculative process. As discussed in following paragraphs, we will bypass this difficulty by assigning an effective melt layer temperature closer to the melting temperature.

5.4. Layer Temperatures:

Here we define the following layer temperatures:

Fluid Layer Temperature: The characteristic melt temperature that one would evaluate the material properties is expected to be somewhere between the melting temperature and the "surface" temperature that separates the high density fuel from the low density gases in the port. We will use the following temperature as the characteristic melt layer temperature for the fuel of interest.

$$T_{melt} = \frac{T_s + 2T_m}{3} \tag{94}$$

We believe that variations in the specific definition of the layer temperature would change the numerical value of the entrainment parameter constant K, but most likely would keep the shape of the regression rate distribution invariant. Thus, it is expected that this simplified approach would be accurate to compare the relative burn rates of fuel formulations.

Solid Layer Temperature: We will use the following temperature as the characteristic solid layer temperature for the fuel of interest.

$$T_{solid} = \frac{T_a + T_m}{2} \tag{95}$$

6. Pyrolysis Data for n-Alkanes:

As shown in section 5.3, the surface temperature estimation under the supercritical regime requires the knowledge of the pyrolysis parameters such as the activation energy and the rate constant for the fuel of interest. In this section we will summarize the information gathered from the chemical kinetics literature on the pyrolysis of n-alkanes for a range of carbon numbers from butane ($n=4$) to the HDPE polymer[28, 29, 30, 31, 32]. The majority of these studies focus on reactions of the zeroth or first order for the thermal decomposition process.

For the sake of simplicity, we will only consider the first order pyrolysis reaction which can be expressed as

$$\frac{dY_f}{dt} = -k_p(T, P_c, n)Y_f . \tag{96}$$

In general, the reaction constant, k_p, is a function of the temperature, pressure and the carbon number. Typically, the temperature dependency of the rate function can be written in the Arrhenius form as

$$k_p(T, P_c, n) = a_t(P_c, n) \ e^{-E_a/R_u T} . \tag{97}$$

Here E_a is the activation energy for the pyrolysis reactions. For the pressure and carbon number dependency, we refer to the data given in Ref. 28 to evaluate $a_t(P_c, n)$ for the carbon number range of 4-32.

$$\text{If } 4 \leq n \leq 11 \qquad a_t(P_c, n) = 10^{12}[1 + 0.0259(P_c - 1)] \ (n - 1) \ (1.57n - 3.9) \tag{98a}$$

$$\text{If } 11 \leq n \leq 32 \qquad a_t(P_c, n) = 10^{13}[1 + 0.0259(P_c - 1)] \ (2.3n - 15.6) \tag{98b}$$

Note that the pressure is in atmospheres and the rate constant is in 1/sec. The rate data given by Eqs. 98a and 98b are calculated for an activation energy of 60 kcal/mole as reported in the literature[28] for alkanes with carbon numbers larger than 3. The experimental findings discussed in Ref. 28 also suggests that the

effect of pressure on the activation energy for pressures less than 40 atmospheres is negligible.

Similarly using the thermal degradation data from Refs. 31 and 32, we have evaluated the rate constant for the polyethylene polymer.

If $n \rightarrow \infty$ $\quad a_t(P_c) = 10^{18}[1 + 0.0259(P_c - 1)]$ (98c)

Note that we have retained the pressure function for convenience. It has been determined that an activation energy of 60 kcal/mole also fits the polymer data

reasonably well and should be used with the rate constant given by Eq. 98c.

The gap in the data for the pyrolysis rate constants has been filled using the following interpolation formula

$$\text{If } 32 < n < \infty \qquad a_t(P_c, n) = 10^{15}[1 + 0.0259\ (P_c - 1)]\ \left(2.91 - 2.093\ e^{-0.01(n-32)}\right).$$ (98d)

Pyrolysis rate constants as a function of the carbon number have been plotted in Figure 10 for three pressures values. Note that the pyrolysis rate increases with increasing carbon number as the longer molecules become more vulnerable to the bond scission reactions. Pressure also increases the rate constant.

The pyrolysis data discussed in the previous paragraphs is for bulk pyrolysis (as in the thermogravimetric analysis) at fairly slow heating rates, typically 0.1-1 K/sec. Whereas the processes that take place in hybrid rockets involve heating rates that are several orders of magnitude larger (i.e. 10^2-10^4 K/sec). The effect of the heating rate on the pyrolysis of polymers has been studied and reported in the literature (for example see Ref. 27 for Hydroxyl-Terminated Polybutadiene). The primary effect of the increase in the heating rate has been shown to reduce the activation energy. Unfortunately, to the best of our knowledge, rapid pyrolysis data for the series of n-alkanes does not exist. We have decided to take the simple approach of modifying the activation energy based on matching the surface temperature for the HDPE polymer predicted by the theory to the surface temperature values commonly observed in polymeric hybrid fuels (i.e. 800 K). This simple method resulted in an activation energy of 45 kcal/mole and a surface temperature of approximately 812 K. Note that the use of the slow rate activation energy 60 kcal/mole yields an unrealistically high surface temperature of 950 K.

The other important key information needed in the liquid layer hybrid combustion model is the heat of pyrolysis, namely the heat required to thermally

decompose a unit mass of fuel. The estimation of the heat of pyrolysis requires information on the composition of the end products of the pyrolysis reactions. Typically, the thermal degradation of the normal paraffin molecules does not result in large concentrations of the monomer (ethylene)[28, 29]. Depending on the carbon number of the original fuel and the pyrolysis conditions, the products are composed of a range of lower n-alkanes, n-olefins and some branched hydrocarbons. The detailed composition of the end products can be approximated using the Rice-Kossiakoff theory[28]. For the purposes of this paper, we will bypass this complex, free radical based pyrolysis model and simply assume a final product distribution that is composed of one type of alkane and 1-olefin molecules with a preset carbon number, n_e, that characterizes the real decomposition products. Based on this simple argument, the pyrolysis reaction can be written as

$$C_nH_{2n+2} \xrightarrow{q_p} N_a C_{n_e}H_{2n_e+2} + N_o C_{n_e}H_{2n_e}.$$ (99)
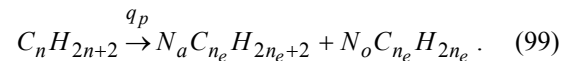
For the specific case of $n_e = 5$ this reaction becomes

$$C_nH_{2n+2} \xrightarrow{q_p} C_5H_{12} + (0.2n - 1)\ C_5H_{10}.$$ (100)
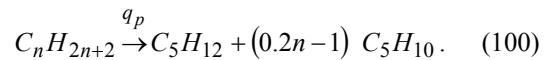
Based on this simplified pyrolysis reaction, the heat of pyrolysis can be approximated as

$$\hat{q}_p = \left[\Delta\hat{H}_{f,298}^{IG} + \hat{C}_g(T_s - 298)\right]_{C_5H_{12}} + (0.2n-1)\left[\Delta\hat{H}_{f,298}^{IG} + \hat{C}_g(T_s - 298)\right]_{C_5H_{10}} - \left[\Delta\hat{H}_{f,298}^{IG} - \hat{L}_{v,298} + \hat{C}_l(T_s - 298)\right]_{C_nH_{2n+2}}.$$ (101)

Here $\Delta\hat{H}_{f,298}^{IG}$ is the heat of formation of the ideal gas at 298 K, $\hat{L}_{v,298}$ is the heat of vaporization at 298 K, $\hat{C}_l$ is the molar heat capacity of the liquid and the

$\hat{C}_g$ is the molar heat capacity of the gas. Note that all of these properties can be estimated using the ABC method[20,21, 22]. We have assumed that at the surface temperature, the pyrolysis products are in the gaseous phase, which turns out to be a good assumption for the

relatively high surface temperatures calculated for n-alkanes (i.e. for the supercritical case heat of vaporization is zero). The mass based heat of pyrolysis can easily be calculated using the relation

$$q_p = \frac{\hat{q}_p}{Mw} . \qquad (102)$$

7. Estimation of the Heat of Formation:

The heat of formation of the solid alkane at a specified ambient temperature is required for the thermochemical calculations (i.e. calculation of c*). It is also used in the estimation of the effective heat of gasification, which will be discussed in the following section. The molar heat of formation of the solid at a temperature T_a, which is lower than the melting temperature, can be written as

$$\Delta \hat{H}^s_{f,Ta} = \Delta \hat{H}^{IG}_{f,298} - \hat{L}_{v,298} - \hat{L}_m - \hat{C}_s \left(298 - T_a \right) \quad (103)$$

Using the ABC method, we have estimated the molar heat of formation (in kcal/mole) of the solid alkanes as

$$\Delta \hat{H}^s_{f,Ta} = -6.713n - 7.846 - \hat{C}_s \left(298 - T_a \right) . \quad (104)$$

The mass based heat of formation of the solid becomes

$$\Delta H^s_{f,Ta} = \frac{\Delta \hat{H}^s_{f,Ta}}{Mw} . \qquad (105)$$

Eq. 105 indicates that the heat of formation decreases with increasing carbon number. Consequently, the c* and Isp performance drops with growing n within the series of n-alkanes. The decrement in the performance diminishes with increasing carbon number and for carbon numbers larger than 15 there is no practical difference in the c* values of the compounds. We would like to note that n-alkanes have the best c* and Isp performance within the family of hydrocarbons because of their superior hydrogen to carbon ratio.

8. Estimation of the Effective Heat of Gasification:

The heat of gasification is defined as the heat required to take one mole of fuel at its ambient conditions and bring it to the thermodynamic state of the gas at the surface temperature. In the subcritical regime this can be written as

$$\hat{h}_v = \left[\Delta \hat{H}^{IG}_{f,298} + \hat{C}_g \left(T_s - 298 \right) \right]_{C_nH_{2n+1}} - \left[\Delta \hat{H}^s_{f,298} \right]_{C_nH_{2n+1}} . \qquad (106)$$

In the supercritical case the effective heat of gasification takes the following form

$$\hat{h}_v = \left[\Delta \hat{H}^{IG}_{f,298} + \hat{C}_g \left(T_s - 298 \right) \right]_{C_5H_{12}} + \left(0.2n - 1 \right) \left[\Delta \hat{H}^{IG}_{f,298} + \hat{C}_g \left(T_s - 298 \right) \right]_{C_5H_{10}} - \left[\Delta \hat{H}^s_{f,298} \right]_{C_nH_{2n+1}} \qquad (107)$$

The mass based heat of gasification of the solid becomes

$$h_v = \frac{\hat{h}_v}{Mw} . \qquad (108)$$

9. Motor Tests:

A large set of motor test data already exits for the following n-alkane-based hybrid fuels.

- Paraffin Wax FR5560 (Also referred to as SP-1a): This is a fully refined paraffin wax with a melting point of approximately 70 C. FR 5560 has been used as the base material for the paraffin-based fuel formulation, SP-1a that has been developed as a fast burning hybrid rocket fuel[8, 11, 12]. An extensive number of tests (up to 6,000 lbf class motors[13]) have been conducted with this particular formulation using various oxidizers such as GOX, LOX and N_2O.

- Pentane: Pure C_5H_{12} solidified at liquid nitrogen temperature (77 K) has been burned with gaseous oxygen. The detailed description of the motor tests conducted by AFRL is given in references 2, 3 and 4 and the reduced regression rate data used in this paper has been reported in reference 9.

In order to establish the burn rate characteristics of the entire homologous series of n-alkanes, more small motor tests have been conducted using various new

23

paraffinic fuel formulations with varying average molecular weights and polydispersities. The testing effort has been limited to 3-4 tests per new formulation. With this limited testing program, it has been possible to quantify the general level of burning rate for each formulation compared to the HDPE polymer, but more testing is needed to completely establish the internal ballistics for each of these new paraffinic fuels.

Test Facility: All tests are conducted using a 3" OD hybrid motor which runs with gaseous oxygen as the oxidizer. The grain OD is limited to 5.84 cm (2.3" inches) and the length can be varied by swapping the combustion chamber tube. The motor is ignited using a methane oxygen torch which lasts for approximately 0.3 seconds. The nominal burn time is 3 seconds for all tests.

The oxygen flow rate is initiated by opening a series of Aktomatic solenoid valves. The motor and the chamber are isolated from each other by a sonic orifice which operates in the choked condition for all motor tests. A pressure transducer collects data at the upstream end of the sonic orifice, which is used to calculate the mass flow rate for each test. The sonic orifice has been calibrated and the discharge coefficient for the orifice is determined to be 0.83, which is in good agreement with the value 0.84 quoted in the literature for square edge orifices operating under choked conditions[33].

The 3 inch facility utilizes ATJ graphite nozzles with no divergent section. The nozzle erosion rates for all the tests reported in this paper has been negligible. The motor is controlled remotely by a Labview VI designed particularly for the 3 inch facility. The chamber pressure and the feed system pressure are measured using Kistler 601B1 pressure transducers. These transducers have been factory calibrated and supplied with the calibration curves. The pressure signals are amplified using Kistler charge amplifiers with long time settings making these transducers capable of operating in a quasi-steady mode over the duration of the test. The data is collected at a slow rate, typically less than 100 Hz, for most of the tests. The slow sampling rate has been adequate for motor tests tailored to characterize the burn rate of different fuel formulations. The details of the facility are discussed in Ref. 8.

We would like to note that this facility has been extensively used to evaluate paraffin-based fuels, especially the baseline fuel SP-1a (more than 200 tests have been conducted with various paraffin formulations). For SP-1a, the regression rate data obtained from the 3 inch motor showed excellent agreement with the set of data obtained from the 10

inch motor tests conducted at the Hybrid Combustion Facility of NASA Ames Research Center[13].

The fuel grains which are fabricated by either casting or machining are cartridge loaded into the motor casing. The insertion and removal of the fuel grains has been achieved without difficulty due the reasonably large tolerance between the grain OD and the motor case ID. In order to prevent outside combustion, insulators at both ends have been inserted between the grain and the casing.

Data reduction and error analysis methods used in this paper are reported in reference 13.

New Fuel Formulations:

The following are the new paraffinic fuel formulations that have been tested and will be reported in this paper:

- Paraffin Wax FR4045 : A fully refined paraffin wax grade with a melting point of approximately 61 C. A small fraction of a high absorptivity material has been added to minimize the radiative thickness. Fuel grains used in the motor tests have been cast centrifugally.
- Polyethylene wax (Marcus 200): This polyethylene wax has been acquired from Marcus Oil & Chemical Company in the form of small pellets. The number averaged and weight averaged carbon numbers are reported by the vendor to be 79 and 134 respectively, resulting in a polydispersity of 1.71. Based on the number averaged carbon number the melting point is estimated to be approximately 110 C (fairly close to the peaks observed in the DSC traces as reported by the vendor). A small fraction of a high absorptivity material has been added to minimize the radiative thickness. Fuel grains used in the motor tests have been cast in axial layers and then machined to the specified port diameter and length. The outside surface of the grains is not machined.
- Polyethylene wax (Polyflo 200): This polyethylene wax has been acquired from the Munger and Moore Company in the form of small pellets. For this particular grade reliable number averaged and weight averaged carbon numbers could not be obtained. We have measured the melting point to be approximately 102 C, resulting in a number averaged carbon number of 62. A small fraction of high absorptivity material has also been added to Polyflo 200 in order to increase its radiation absorption capability. Fuel grains used in the motor tests have been cast in axial layers and then machined to the specified port diameter and

length. The outside surface of the grains is not machined.

- High Density Polyethylene Polymer: This material has been purchased from Interstate Plastics Inc. in the form of cylindrical rods. The molecular weight distribution for this particular polymer could not be obtained. However the high density, high melting point and the extremely high melt viscosity indicates a high molecular weight most likely larger than 100,000 g/mole. Fuel grains are produced by machining the plastic material.

Discussion of Test Results: Tables 2a and 2b summarize the motor test parameters and important test results such as the average regression rate and average oxidizer mass flux.

Figure 11 shows the pressure time traces for a typical test. The feed system and chamber pressures are fairly constant and the orifice is certainly choked for the entire test. The figure also shows smooth ignition with no overshooting which indicates that the effect of the ignition pulse on the regression rate is negligible. The effective burn time, which is defined from the middle of the ignition transient to the middle of the thrust termination transient, is also marked in the figure. It has been determined that the burn time for all the tests reported in this paper is 3.0 seconds with a 0.1 second variation.

All motor tests were successful and included in data reduction to produce regression rate data. Tests 13 and 14 had anomalous chamber pressure measurement and the pressures for these tests have not been reported. For all the runs, the combustion was stable. Namely, the pressure time traces were reasonably smooth as seen in Figure 11 and the plumes were observed to be steady. We did not make any attempt to quantify the stability character of the motors tested in this study.

Figure 12 shows the regression rate as a function of oxidizer mass flux for all of the motor tests conducted under in this investigation. We have also included the well established regression rate law for the baseline fuel, SP-1a, given by the following expression[13].

$$\dot{r} = 0.488 G_{ox}^{0.62} \qquad (109)$$

Here the flux is in g/cm²-sec and the regression rate is in mm/sec. The data points for SP-1a have been excluded from the plot to make room for the data obtained from the new tests. For the purposes of this paper we will assume that all formulations have the same flux exponent and the regression rate is solely determined by the mass flux coefficient. This is probably a reasonable approach if the mass flux used in

the calculations matches the range of fluxes for which the tests were conducted.

As expected, the HDPE polymer is the slowest burning alkane with a burn rate of approximately 20 % of SP-1a regression rate. Note that the low flux data point for the HDPE polymer is slightly above the fit that uses a mass flux exponent of 0.62, indicating that a lower exponent would fit the data better. In order to verify this observation more tests must be conducted at the low end of the mass flux spectrum.

Figure 12 also shows that the PE waxes Polyflo 200 and Marcus 200 burn approximately 4 and 3 times faster than HDPE, respectively. Finally the lighter alkanes pentane and low grade paraffin wax FR4550 regression rate are approximately 5.5 and 5.4 times the regression rate of the polymer. Table 3 summarizes the relative regression rates for all alkanes discussed in this section.

10. Discussion of Results:

The enhanced liquid layer combustion theory outlined in section 3 has been applied to the homologous series of normal alkanes. The only parameter that can be freely adjusted is the coefficient of the entrainment parameter, K which has been selected to be 1.421×10^5 m$^{4.4}$-sec$^{1.4}$/kg$^{2.4}$ in order to match the theory prediction to the observed regression rate for the baseline fuel SP-1a.

Figure 13 shows the theory predictions for the non-dimensional regression rates as a function of the carbon number in the range of 5-1000. The member of the series with carbon numbers less than 5 have not been considered in this study since they have little practical importance in hybrid applications and only limited experimental data is available for such materials. The following selection of the variables has been used in the construction of the regression rate plots in the supercritical operating regime.

$$E_a = 45 \ kcal/mole, T_p = T_s - 100 \ K$$
$$Y_{fs} = 0.01, \ \dot{r} = 0.001 \ m/\sec$$

Here the regression rate is assumed to be a constant value that is used to estimate the surface temperature at the onset of the entrainment process. It has been shown that varying its value (within a practically acceptable range) does not affect the end result significantly. As discussed in the previous section, the activation energy is selected based on the expected surface temperature for the polymer and is assumed to be constant for all members of the series. We have determined that the effect of reasonable variations in the extent of pyrolysis

at the surface and the value of T_p on the end result is negligible. Furthermore, the chamber pressure has been assumed to be 20 atm in order to match the experimental conditions as close as possible for all materials reported in section 9. The melt layer thickness expressions for the very high radiative absoptivity case, $R_l >> 1$, have been used for all materials. Finally each fuel is assumed to be a pure n-alkane with the corresponding carbon number. Mixtures will be discussed later in this section.

Figure 14 shows the variation of the important temperatures as a function of the carbon number. The ambient temperature has been assumed to follow the selected variation discussed in section 5. The melting temperature increases monotonically and continuously with the carbon number. The rate of increase diminishes as the carbon number increases. The critical temperature also follows a similar behavior. Namely, it increases monotonically with a decreasing rate. As expected, the most complicated behavior is in the surface temperature. In the subcritical region, the surface temperature is determined by the physical process of evaporation and it increases with increasing carbon number. Note that in the subcritical operating regime, the theory correctly predicts a surface temperature less than the critical temperature for that particular carbon number. Since the critical pressure decreases with the carbon number, at a certain n the partial pressure of the vapor at the surface becomes equal to the critical pressure for this particular n-alkane. This is the critical carbon number beyond which the distinction between the liquid and gas disappears and the supercritical operation takes over. Since the definition of the surface and the conditions determining the surface temperature in the supercritical regime are completely distinct from the subcritical case, a significant jump in the surface temperature at the critical carbon number has been observed. It is shown in the figure that the surface temperature determined by the pyrolyis process is much higher than the temperature dictated by the evaporation process. In the supercritical regime, as the carbon number further increases the surface temperature starts to decrease with a diminishing rate. The drop in the temperature, the opposite trend compared to the evaporation case, is due to the increase in the rate coefficient with increasing carbon number. Namely the normal alkane molecules are becoming less resistant to thermal decomposition as they become longer. The surface temperature asymptotes to a value close to 812 K for the case of infinitely long chain polymer. Finally the effective fluid layer temperature is also plotted in Figure 14 as it is defined by Eq. 94. The fluid layer temperature increases in the low end of the carbon numbers and stays fairly constant in the supercritical regime for the moderate to high carbon numbers. Note

that this is the temperature that the fluid properties are evaluated to estimate the entrainment parameter.

Figure 15 shows the variation of the effective heat of gasification and its components as a function of the carbon number. The effective heat of gasification increases in the subcritical region and jumps to a much higher value once the critical carbon number is reached. The energy components that derive the increase in the heat of gasification are the heat of pyrolysis, which is only nonzero in the supercritical case, and the increase in the liquid heating due to the sudden jump in the surface temperature. In the supercritical regime, the effective heat of gasification declines slowly and asymptotes to a value of 782.1 cal/g for the infinite chain polymer. The change in the value of the effective heat of gasification within the subcritical and supercritical regions is reasonably small. Also note that the heat of pyrolysis is zero in the subcritical regime and increases in the supercritical regime to its asymptotic value of 412.1 cal/g as the carbon number goes to infinity. The heat of vaporization is only nonzero in the subcritical regime. It has been observed that the heat of vaporization decreases with increasing chamber pressure and it should diminish as the critical pressure is reached. The heat of melting and solid heating are small compared to the other components. They also increase with increasing carbon number over the whole range of carbon numbers.

One of the key consequences of the change in the effective heat of gasification is its influence on the blowing parameter. In fact, the blowing parameter as calculated by Eq. 24 is plotted in Figure 16. The value of the blowing parameter decreases from approximately 13 in the subcritical regime to a value of roughly 5 in the supercritical case. The variation of B has paramount importance since it significantly influences both the classical regression rate and also the entrainment parameter.

As indicated by Eq. 23, the entrainment parameter strongly depends on the properties of the fluid layer evaluated at the effective melt layer temperature. The key properties that explicitly affect the entrainment parameter (the viscosity, liquid density and the thickness parameter) are plotted in Figure 17 . As expected, the viscosity shows a decreasing trend with increasing carbon number. The sharp change in the slope of the viscosity curve at the carbon number of 250 is due to the entanglement transition of the long chain alkane molecules as discussed in section 4. The sharp changes in the density and the thickness values at the carbon number of 12 are induced by the transition from the subcritical to supercritical operation.

Figure 18 shows the plot of the entrainment parameter, R_{ent}, as a function of the carbon number. In order to match the experimental conditions, we have used the characteristic values of $\dot{Q}_r/\dot{Q}_c = 0.1$ $G=100$ kg/m^2-sec and $z=0.1$ m in evaluating the entrainment parameter. We would like to note that due to the low exponents of the G and z, we believe that the effect of variations in these variables on the end result is expected to be small. As indicated by the figure, the entrainment parameter is low in the subcritical region mainly due to the high value of the blowing parameter. R_{ent} jumps to high value as the critical carbon number is reached and it starts to decrease with increasing carbon number. A quick study of Figures 2 and 5 reveals that the decline in R_{ent} is driven by the increase in the melt layer viscosity, showing the importance of viscosity in determining the regression rate behavior, at least in the supercritical operating regime.

As discussed earlier in this section, the non-dimensional components of the regression rate are calculated for each carbon number and plotted in Figure 13. First, it has been observed that the classical regression rate drops from the subcritical regime to the supercritical regime. This variation is induced by the change in the blowing parameter. Note that the classical regression rate of the infinitely long chain polymer has been taken as the reference point, and the classical regression rates corresponding to all other carbon numbers are normalized with respect to the reference. The entrainment regression rate follows the trend of the entrainment parameter very closely. Namely, the entrainment regression rate in the subcritical region is low due to the low values of the entrainment parameter. At the critical point, the entrainment regression rate jumps to a high value and starts to decrease with the growing carbon number as the layer becomes more viscous. The total non-dimensional regression rate that is normalized with respect to the local classical regression rate follows the entrainment regression rate closely. Figure 13 indicates that the changes in the vaporization component of the regression rate are minor compared to the variation in the entrainment part. Non-dimensional vaporization regression rate slowly asymptotes to the value of one as the entrainment regression rate diminishes at very large carbon numbers. The figure also shows that at $n=1000$ the total regression rate is very close to its classical value. In fact it is expected that at a certain carbon number the fluid film would be stabilized and the entrainment component would suddenly drop to zero. Even though the onset boundary for the entrainment mass transfer has not been investigated in this paper, it is expected to be at a carbon number larger than 300, which is well beyond the practical range for fast burning hybrid fuels. The total non-dimensional regression rate with respect to the polymer (which is $\dot{r}/(\dot{r}_{cl})_{ref} = \phi_{cl}\phi$) is also shown in Figure 13. Note that the effect of the blowing parameter on the classical regression rate and the entrainment regression rate compensate each other to a high degree, and result in a fairly smooth transition in the total regression rate, $\dot{r}$, as the operation moves from the subcritical into the supercritical regime.

So far in the discussion of the theory predictions, we have assumed that each fuel formulation is composed of a single n-alkane component. In reality almost all practical paraffinic solid fuels, such as paraffin waxes, PE waxes or polymers are mixtures of n-alkanes. As discussed in section 4, for the purposes of this paper we will simply assume that all material properties, other than viscosity, can be evaluated at the number averaged carbon number, whereas the viscosity should be evaluated at the weight averaged carbon number. It has been shown in Ref. 25 that this is a fairly accurate assumption for the mixtures of paraffins and olefins. Based on the preceding simplification, the liquid layer theory can be expanded to treat the mixtures of n-alkanes by introducing the polydispersity (i.e. *PD*), which is defined as the ratio of the weight averaged molecular weight to the number averaged molecular weight. For a pure *n*-alkane the polydispersity is one and it increases as the distribution of the molecular weights in the mixture broadens. In our model, we evaluate all the properties at a carbon number, n, which corresponds to the number averaged carbon number and evaluate the viscosity at the carbon number *n*PD*.

Figure 19 shows the predicted regression rate with respect to the regression rate of the polymer for three values of polydispersity, 1, 1.1 and 1.71. Only the *PD=1* case has been plotted in the figure for the subcritical regime, since these low carbon number materials are often pure liquids (pentane) or liquids with a very narrow cut molecular weight distribution (kerosene). It can be deduced from the figure that as the polydispersity increases, the improvement in the regression rate over the polymer is compromised. This is due to the increased viscosity for a given number averaged carbon number (melting temperature). Thus the best hybrid fuel with a specified melting point is the material with the narrowest molecular weight distribution.

The experimental results for various paraffinic materials have also been included in the figure. As mentioned earlier in this section, the paraffin wax FR5560 (or SP-1a) with a polydispersity of 1.1 has been selected as the reference point. Namely, the entrainment parameter coefficient, *K*, has been selected to match this data point. The error bar for FR5560 is

smaller compared to the others test results reported in the figure due to the vast number of tests conducted with this particular formulation. The regression rate data for the PE wax Marcus 200, which has a polydispersity of 1.71, is in very good agreement with the liquid layer prediction. The fit for the other PE wax, Polyflo 200, is not as good. The position of the data point suggests that the polydispersity for this particular material is 1, which is a fairly unrealistic deduction. Even though no reliable polydispersity data is available for this particular PE wax, it is expected to be more than the polydispersity of the paraffin wax FR5560.

The regression rate prediction for the lower grade paraffin wax FR4045 is also very accurate. The prediction is well within the error bounds of the test result. The data point suggests a polydispersity slightly less than the polydsipersity of the FR5560 which is certainly plausible.

The theory estimates the regression rate for pure pentane, which is operating in the subcritical region, with reasonable accuracy. The prediction is slightly higher than the experimental data point and this minor deviation is probably due to the effect of the small but finite surface tension on the entrainment mass transfer which has been ignored in the current model. We also would like to note that the pentane tests were conducted in a less controlled environment due to the cryogenic nature of the propellant and the certainty in the experimental results is not as high as it is for the non-cryogenic fuels considered in this study.

We have also investigated the effect of the chamber pressure on the theory predictions. In the subcritical region, increasing pressure reduces the latent heat of vaporization and increases the surface temperature. The effect of pressure on the regression rate in the subcritical regime is determined to be small but finite. It has been determined that the primary influence of pressure is to shift the critical carbon number, namely the critical carbon number decreases with increasing pressure. The effect of pressure in the supercritical regime has been predicted to be negligible. This observation is in good agreement with the deductions from the extensive motor test data for the baseline fuel SP-1a. Specifically, the regression rate of SP-1a showed no distinguishable dependency on the chamber pressure in the broad range of 2-68 atm[13].

The thickness of the reaction zone with respect to the characteristic thickness of the liquid layer has been plotted in Figure 20 for the entire series of n-alkanes. Note that the relative thickness is always less than 0.05 which validates the assumption introduced in estimating the surface temperature in section 5.3.

In Figure 21 we show the variation of the surface tension as a function of the carbon number. The two important observations are that the surface tension values are fairly small for the chamber pressure used in this example case and the changes in the surface tension are small within the subcritical range of carbon numbers. Both of these conditions verify the exclusion of the surface tension from the entrainment mass transfer scaling law. Also note that the surface tension in the supercritical case is shown to be zero since the surface is defined by the pyrolysis chemistry not by phase change.

11. Conclusions

The following are the conclusions:

- The liquid layer combustion theory has been improved. The regression rate equations are cast in a non-dimensional format. A non-dimensional universal regression rate law has been developed for liquefying fuels that are characterized by entrainment mass transfer along with vaporization mass transfer. Examining Eqs. 16, 20 and 23 indicate that, the mass flux exponent for the entrainment part of the regression rate is slightly higher than the classical flux exponent, and the length exponent for the entrainment component is approximately zero. Note that the classical theory predicts a negative length exponent of -0.2. The lack of significant dependency on the grain length is in agreement with the results of motor tests conducted at different scales[13].

- The surface temperature has been estimated for the subcritical and also for the supercritical operating conditions. Even though a large jump in the surface temperature has been observed at the critical carbon number for which the transition takes place, the regression rate prediction is a relatively smooth function of the carbon number. In the supercritical region the effect of chamber pressure on the regression rate is determined to be negligible. This observation is also in very good agreement with the experimental results.

- The improved liquid layer theory has been applied to the homologous series of normal alkanes. The predicted regression rates agree well with the motor test data obtained from several paraffinic fuel formulations covering a wide range of carbon numbers: liquid pentane, paraffin wax 4550, paraffin wax 5560, PE wax Polyflo 200, PE wax Marcus 200 and HDPE polymer. The good agreement between the theory and the test results over a wide range of carbon numbers indicates that the implemented entrainment scaling law is reasonably accurate. It has also been determined that, especially in the supercritical operation

regime, viscosity is the most important variable that dictates the regression rate behavior of a fuel system. Another important outcome of the theory is that the narrow cut mixtures of n-alkanes are most suitable as hybrid rocket fuels, since they present the fastest burning rate for a specified melting temperature.

- The results of this paper show that, for most applications, the paraffin waxes have the best properties as hybrid rocket fuels among the series of n-alkanes due to their fast regression rates at relatively high melting temperatures.
- The theory can easily be applied to the other homologous series such as normal alcohols or normal acids. We believe that the regression rate characteristics for the heavy members of these series will be quite similar to that of the series of n-alkanes since, as the carbon number increases, most properties for different homologous series converge.

The following are some of the areas where further improvement would be beneficial:

- Development of a physics based non-dimensional entrainment mass scaling law. Cold flow experiments and numerical simulations would be necessary to guide this effort.
- Development of a fuel pyrolysis data base for n-alkanes at high heating rates that are observed in rocket applications.
- Construction of the generalized state equations for the series of n-alkanes.
- Development of a more accurate, high fidelity model for the classical regression rate.

12. Acknowledgments

13. References

[1]Marxman, G. A., Wooldridge, C. E., and Muzzy, R. J. "Fundamentals of Hybrid Boundary Combustion", Progress in Astronautics and Aeronautics, Vol.15, 1964 p 485.

[2]Larson, C. W., Pfeil, K. L., DeRose, M. E. and Carric, P. G., "High Pressure Combustion of Cryogenic Solid Fuels for Hybrid Rockets", AIAA paper No. 96-2594, AIAA/SAE/ASME/ASEE 32 nd Joint Propulsion Conference and Exhibit, July 1996.

[3]Larson, C. W., DeRose, M. E., Pfeil, K. L. and Carric, P. G. "High Pressure Combustion of Cryogenic Hybrid Fuels in a Lab-Scale Burner", Proccedings of the 1996 JANNAF Joint Propulsion Conference,

Albuquerque, NM, December 9-13, 1996, published by CPIA, John Hopkins University.

[4]DeRose, M. E., Pfeil, K. L., Carric, P. G., and Larson, C. W. "Tube Burner Studies of Cryogenic Solid Combustion", AIAA paper No. 97-3076, AIAA/SAE/ASME/ASEE 33 rd Joint Propulsion Conference and Exhibit, July 1997.

[5]Gramer, D., Rice, E., Knuth, W. and Clair, C. St., "Experimental Investigation of a Metallized Cryogenic Hybrid Rocket Engine", AIAA paper No. 98-3509, AIAA/SAE/ASME/ASEE 34th Joint Propulsion Conference and Exhibit, July 1998.

[6]Clair, C. St., Rice, E., Knuth, W., and Gramer, D., "Advanced Cryogenic Solid Hybrid Rocket Engine Developments: Concept and Testing", AIAA paper No. 98-3508, AIAA/SAE/ASME/ASEE 34th Joint Propulsion Conference and Exhibit, July 1998.

[7]Altman, D. and Humble, R. "Hybrid Rocket Propulsion Systems" in Space Propulsion Analysis and Design, McGraw Hill, 1995, p382.

[8]Karabeyoglu, M. A., "Transient Combustion in Hybrid Rockets", Ph. D. Thesis, Stanford University, August 1998.

[9]Karabeyoglu, M. A., Altman, D. and Cantwell, B. J., "Combustion of Liquefying Hybrid Propellants: Part 1, General Theory", *Journal of Propulsion and Power*, Vol. 18, No. 3, p. 610-620, 2002.

[10]Karabeyoglu, M. A., and Cantwell B. J., "Combustion of Liquefying Hybrid Propellants: Part 2, Stability of Liquid Films", *Journal of Propulsion and Power*, Vol. 18, No. 3, p. 621-630, 2002.

[11]Karabeyoglu, M. A., Cantwell, B. J. and Altman D., "Development and Testing of Paraffin-Based Hybrid Rocket Fuels", AIAA-2001-4503, 37th AIAA/ASME/SAE/ASEE Joint Propulsion Conference and Exhibit, Salt Lake City, Utah, July 2001..

[12]Karabeyoglu, M. A., Altman, D., Cantwell, B. J., "High Regression Rate Hybrid Rocket Propellants", U.S. Patent No. 6,684,624 B2, February 3, 2004.

[13]Karabeyoglu, M. A., Zilliac, G., Cantwell, B. J., DeZilwa, S., and Castellucci, P. "Scale-Up Tests of High Regression Rate Paraffin-Based Hybrid Rocket Fuels", *Journal of Propulsion and Power*, Vol. 20, No. 6, p. 1037-1045, 2004.

[14]Craik, A. D. D., "Wind Generated Waves in Thin Liquid Films", *Journal of Fluid Mechanics*, vol. 26, part 2, pp. 369-392, 1966.

[15]Gater, R. A. and L'Ecuyer, M. R. L., "A Fundamental Investigation of the Phenomena that Characterize Liquid Film Cooling", *International Journal of Heat and Mass Transfer* Vol. 13, pp 1925-1939, 1970.

[16]Nigmatulin, R., Nigmatulin, B., Khodzaev, Y. A. and Kroshilin, V., "Entrainment and Deposition Rates in a Dispersed-Film Flow", *International Journal of Multiphase Flow* Vol. 22, pp. 19-30, 1996.

[17]Ishii, M. and Grolmes, M. A., "Inception Criteria for Droplet Entrainment in Two Phase Concurrent Film Flow", *AICh Journal*, vol. 21, no. 2, pp. 308-318, 1975.

[18]Nigmatulin, B. I., Klebanonov, L. A., Kroshilin, A. E., "Heat transfer crisis for process steam-liquid dispersed annular flows under non-stationary conditions", *High Temp. Thermal Phys*. No. 18, 1242-1251, 1980.

[19]Marxman, G. A. "Combustion in the Turbulent Boundary Layer on a Vaporizing Surface", Tenth Symposium on Combustion, 1965, p 1337-1349.

[20]Marano, J. J. and Holder, G. D., General Equation for Correlating the Thermophysical Properties of n-Paraffins, n-olefins and Other Homologous Series. 1. Formalism for Developing Asymptotic Behavior Correlations", *Ind. Eng. Chem. Res*. 36, 1887-1894, 1997.

[21]Marano, J. J. and Holder, G. D., General Equation for Correlating the Thermophysical Properties of n-Paraffins, n-olefins and Other Homologous Series. 2. Asymptotic Behavior Correlations for PVT Properties", *Ind. Eng. Chem. Res*. 36, 1895-1907, 1997.

[22]Marano, J. J. and Holder, G. D., General Equation for Correlating the Thermophysical Properties of n-Paraffins, n-olefins and Other Homologous Series. 3. Asymptotic Behavior Correlations for Thermal and Transport Properties", *Ind. Eng. Chem. Res*. 36, 2399-2408, 1997.

[23]Dauber,T. E., Danner, R. T., "Physical and Thermodynamic Properties of Pure Chemicals, Data Compilation", Taylor and Francis, 1997.

[24] Bicerano, J., "Prediction of Polymer Properties", Marcel Dekker Inc., 1996.

[25]Marano, J. J. and Holder, G. D., Prediction of Bulk Properties of Fischer-Tropsh Derived Liquids", *Ind. Eng. Chem. Res*. 36, 2409-2420, 1997.

[26]Moelwyn-Hughes, E. A., "Physical Chemistry, Permagon Press, 1961.

[27]Esker, D. R. and Brewster, M. Q., "Thermal Pyrolysis of Hydroxyl-Terminated Polybutadiene", *Journal of Propulsion and Power*, Vol. 12, No. 2, p. 296-300, 1996.

[28]McKetta J. J., Jr., "Advances in Petroleum Chemistry and Refining", Chapter 4, Volume 9, Interstate Publishers, New York, 1964.

[29]Westerhout, R. W. J., Waanders, J. , Kuipers, J. A. and van SWaaij, W. P. M., Kinetics of the Low-Temperature Pyrolysis of Polyethylene, Polypropylene, and Polystrene Modeling, Experimental Determination, and Comparison with Literature Models and Data", *Ind. Eng. Chem. Res.*, Vol. 36, p. 1955-1964, 1997.

[30]Stohl, F. V., Qader, Q. A., Assoth, F. E. and Thakur, D. S. , "Thermolysis of Higher Molecular Weight Straight Chain Alkanes (C9-C22), *Ind. Eng. Chem. Res.*, Vol. 26, p. 846-852, 1987.

[31]Madorsky, S. L. and Straus, S., "Thermal Degradation of Polymers at High Temperatures", Journal of Research of the National Bureau of Standards-A. Physics and Chemistry, Vol. 63A, No 3, p. 261-268, November-December 1959.

[32]Madorsky, S. L. and Straus, S., "Thermal Degradation of Polymers as a Function of Molecular Structure", Journal of Research of the National Bureau of Standards-A. Physics and Chemistry, Vol. 53, No 6, p. 361-370, December 1954.

[33]Ward-Smith, A., J., "Critical Flowmetering: The Characteristics of Cylindrical Nozzles with Sharp Upstream Edges", *International Journal of Heat and Fluid Flow*, Vol. 1 No. 3, p. 123-132, 1979.

14. Tables and Figures:

Table 1: ABC method temperature coefficients for viscosity and liquid density.

	Viscosity		Liquid Density	
	ΔY_o	ΔY_∞	ΔY_o	ΔY_∞
A	-602.688	0.0290196	8592.30	12.7924
B	77866.8	-241.023	-85.7292	0.0150627
C	198.006	0.0440959	0.280284	$-1.30794 \ 10^{-5}$
D	$-4.18077 \ 10^{-5}$	$-184891 \ 10^{-7}$	$-4.48451 \ 10^{-4}$	$1.59611 \ 10^{-8}$
E	$-2.49477 \ 10^6$	56561.7	0	0

Table 2a: Summary of motor test data.

Test	Formulation	Initial Port ID (mm)	Oxidizer Flow Rate (g/sec)	Final Port ID (mm)	O/F	Regression Rate (mm/sec)	Ave. Oxidizer Flux (g/cm^2-sec)	Chamber Pressure (atm)
1	HDPE	12.8	45.4	17.0	4.41	0.692	26.1	12.5
2	HDPE	17.0	45.3	20.1	4.87	0.522	16.8	11.8
3	HDPE	22.0	32.8	24.3	5.87	0.381	7.7	7.2
4	HDPE	12.8	32.9	16.2	3.79	0.568	19.9	9.6
5	Marcus 200	22.0	21.8	26.2	2.45	0.714	4.8	5.5
6	Marcus 200	22.1	43.9	27.8	3.23	0.945	9.0	11.5
7	Marcus 200	12.6	38.5	22.5	2.16	1.646	15.8	11.8
8	Marcus 200	15.7	41.0	24.3	2.70	1.428	13.1	10.6
9	PolyFlo 200	22.0	21.0	27.6	1.63	0.935	4.4	5.6
10	PolyFlo 200	22.0	39.9	30.4	1.70	1.400	7.4	10.3
11	PolyFlo 200	11.2	43.0	25.5	1.68	2.393	16.3	11.5
12	Paraf. FR4550	24.0	26.1	31.8	1.34	1.293	4.3	7.0
13	Paraf. FR4550	22.4	47.1	33.9	1.77	1.918	7.6	-
14	Paraf. FR4550	14.3	47.1	30.7	1.48	2.737	11.9	-

Table 2b: Summary of motor test data.

Test	Formulation	Grain Length (cm)	Burn Time (sec)	Nozzle Throat Diam. (mm)	Fuel Mass Burned (g)	Notes
1	HDPE	30.48	3.0	9.78	30.9	Successful Test
2	HDPE	30.48	3.0	9.78	27.9	Successful Test
3	HDPE	30.48	3.0	9.53	17.6	Successful Test
4	HDPE	30.48	3.0	9.91	26.0	Successful Test
5	Marcus 200	17.15	3.0	9.65	26.6	Successful Test
6	Marcus 200	17.15	3.0	9.65	40.8	Successful Test
7	Marcus 200	17.15	3.0	9.65	53.3	Successful Test
8	Marcus 200	17.23	3.0	9.96	45.5	Successful Test
9	PolyFlo 200	17.02	3.0	9.53	38.6	Successful Test
10	PolyFlo 200	17.02	3.0	9.53	70.2	Successful Test
11	PolyFlo 200	17.22	3.0	9.53	76.8	Successful Test
12	Paraf. FR4550	17.10	3.0	9.14	58.4	Successful Test
13	Paraf. FR4550	17.10	3.0	9.14	79.9	Pressure Trans. Failure
14	Paraf. FR4550	17.10	3.0	9.14	95.5	Pressure Trans. Failure

Table 3: Summary of the regression rate data for all fuels.

	Burn Rate Factor Relative to SP-1a	Burn Rate Factor Relative to HDPE
Pentane (C_5H_{12})	1.10	5.5
Paraffin Wax FR 4550	1.08	5.4
Paraffin Wax FR 5560 (SP-1a)	1.00	5.0
PE Wax Polyflo 200	0.80	4.0
PE Wax Marcus 200	0.60	3.0
HDPE Polymer	0.20	1.0
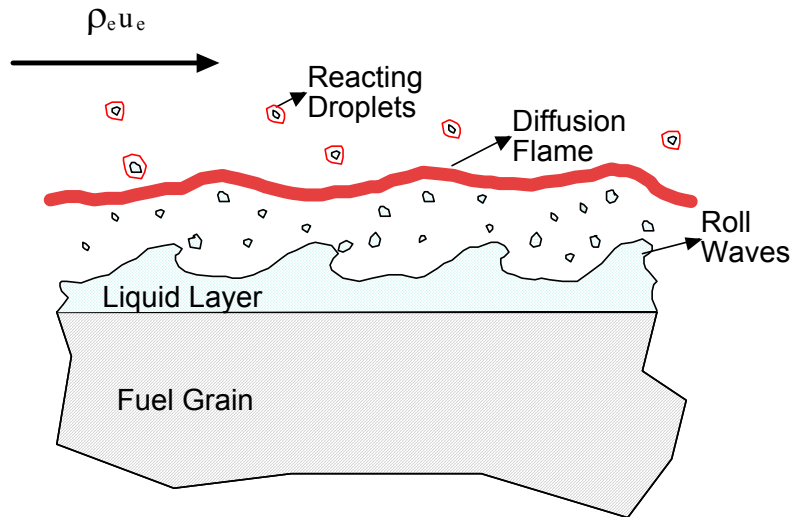
Figure 1: Schematic of the entrainment mechanism
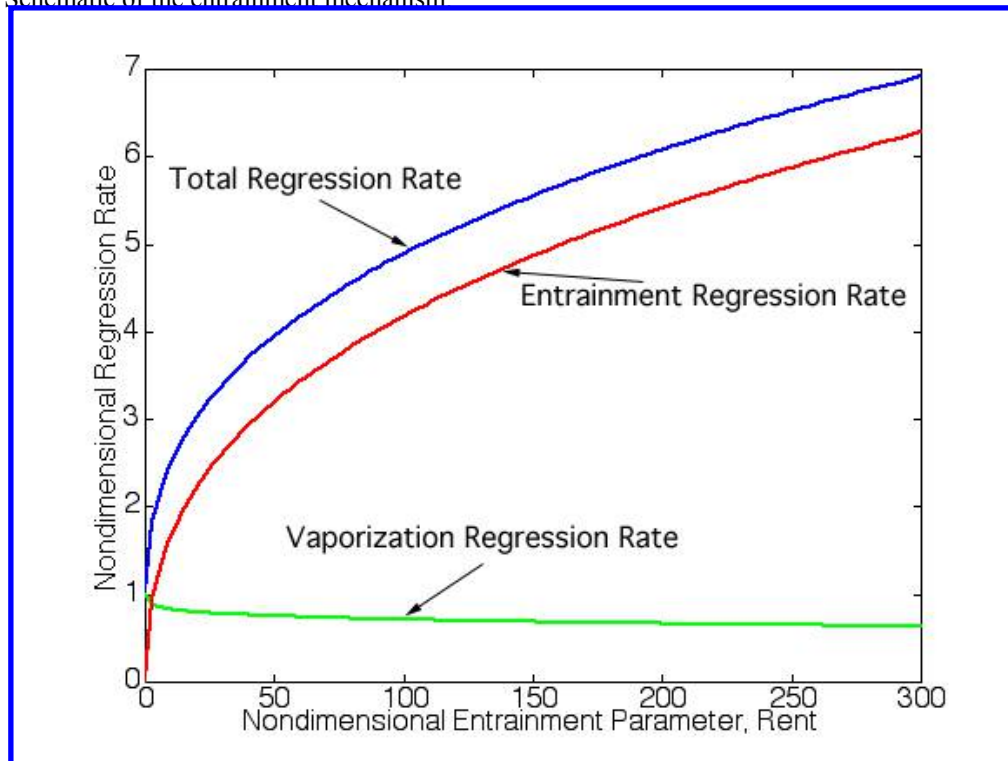
Figure 2: The non-dimensional regression rates as a function of the entrainment parameter has been plotted. The regression rates are normalized with respect to the classical regression rate of this particular fuel formulation. This case is for $\beta = 2$, $B = 4.7$, $R_{hv} = 0.433$ and $R_{he} = 0.051$.
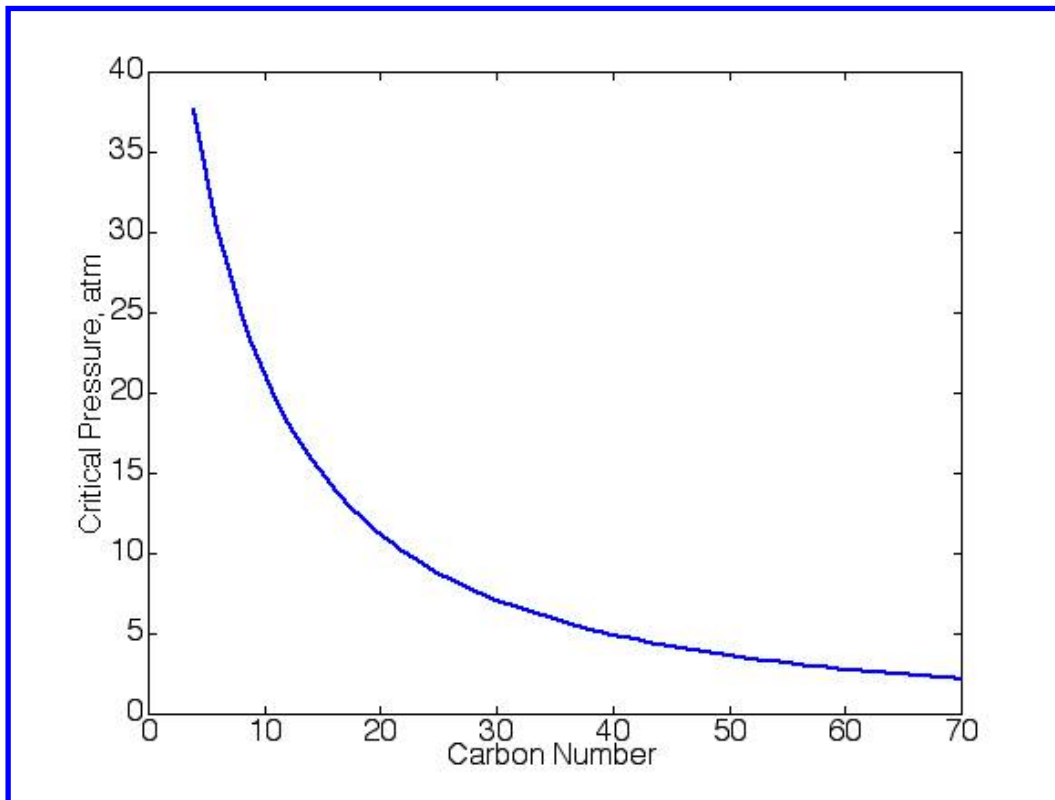
Figure 3: The critical pressure as a function of the carbon number for the homologous series of n-alkanes as predicted by the ABC method
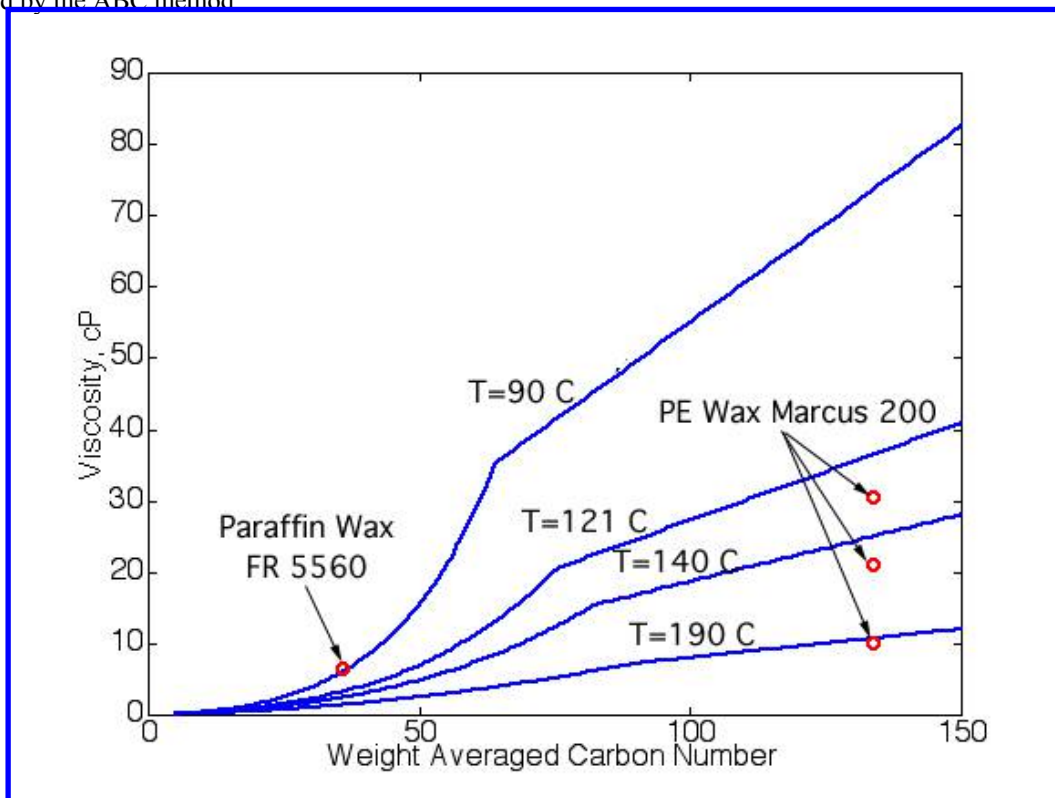
Figure 4: The liquid viscosity as a function of the carbon number for the n-alkanes has been plotted for a range of carbon number and for three temperatures. The viscosity data for the PE wax Marcus 200 and the paraffin wax has also been included in the figure.
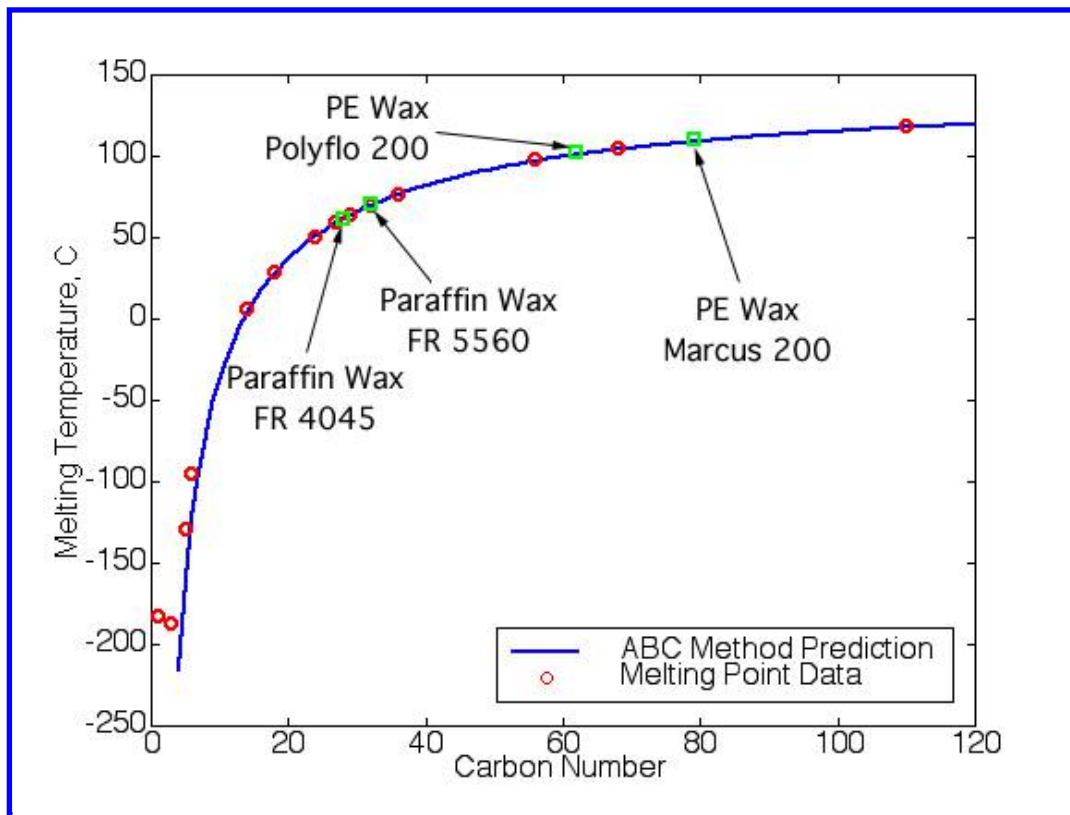
Figure 5: The melting temperature as a function of the carbon number for the homologous series of n-alkanes. The ABC method prediction, solid line, and data points for pure alkanes are included along with the melting points for various paraffin and PE waxes considered in the paper.
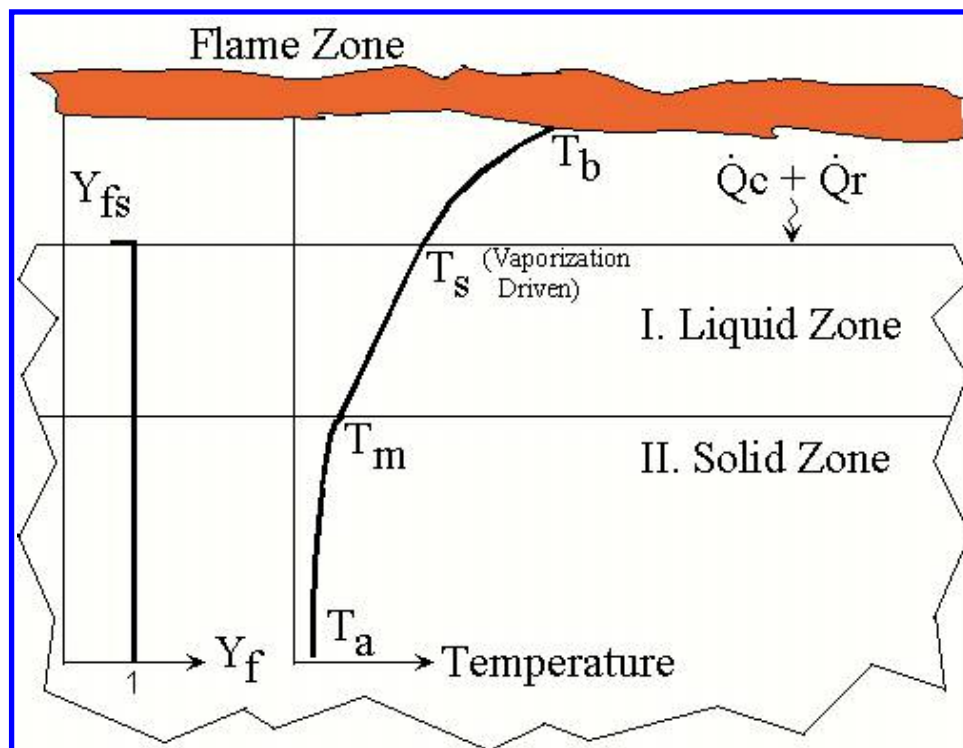
Figure 6a: Schematic of the combustion model for the subcritical regime, $Y_{fs} P_c < P_{cr}$.
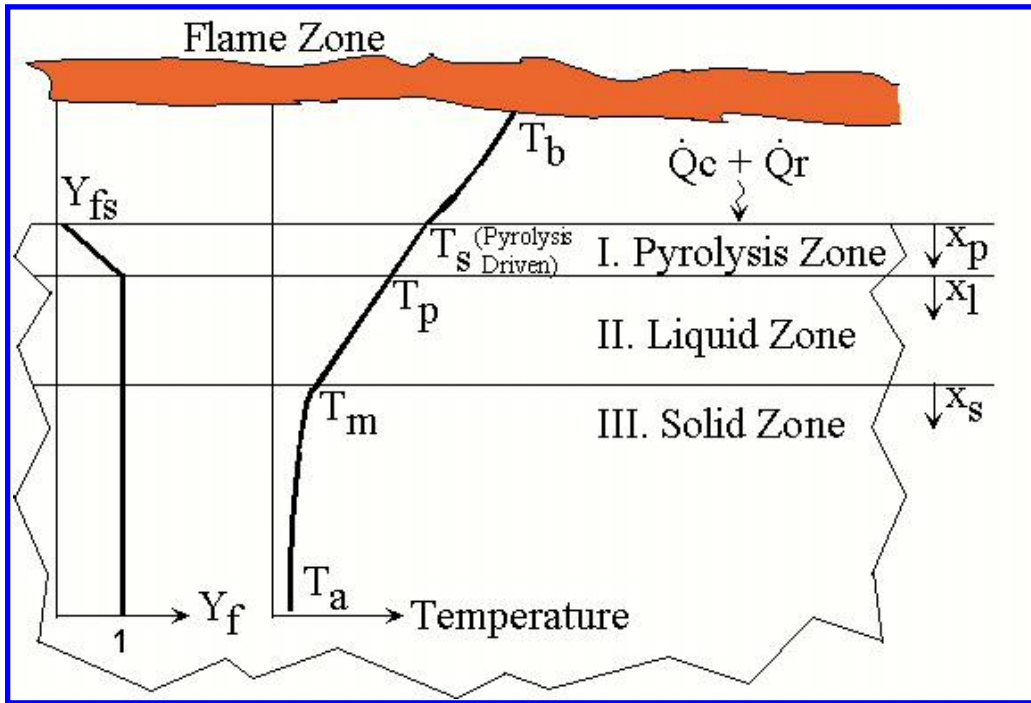
Figure 6b: Schematic of the combustion model for the supercritical regime, $Y_{fs}P_c > P_{cr}$.
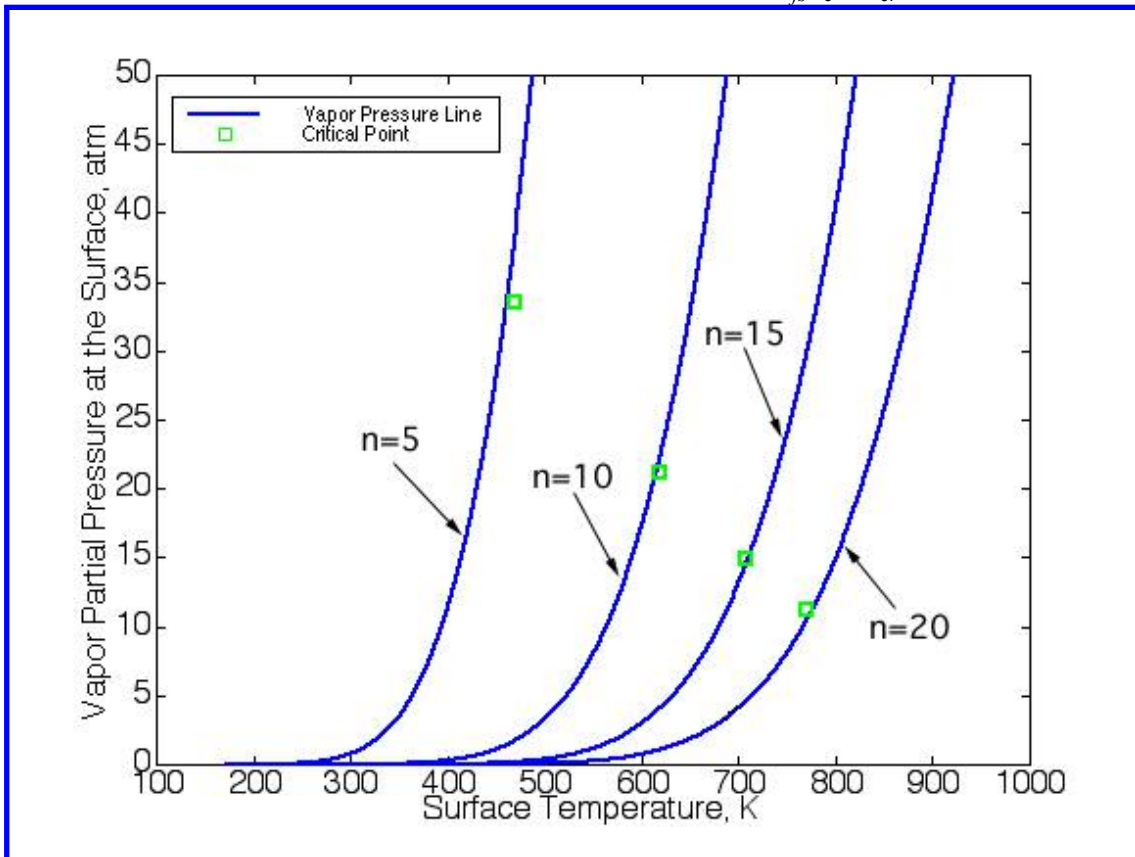
Figure 7: Vapor partial pressure at the fuel surface as a function of the surface temperature for various n-alkanes. Subcritical case.
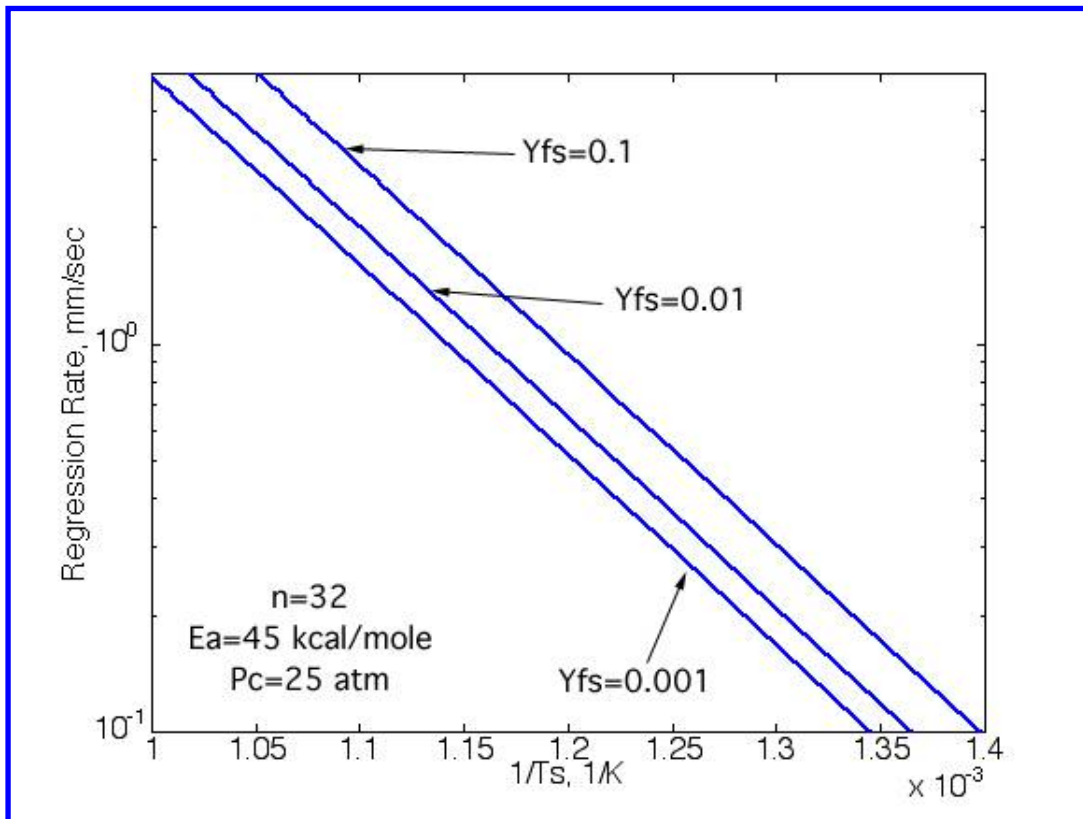
Figure 8: Regression rate as a function of the surface temperature for $C_{32}H_{66}$ at three different fuel mass fraction values at the surface. Activation energy is 50 kcal/mole and chamber pressure is 25 atm. Supercritical case.
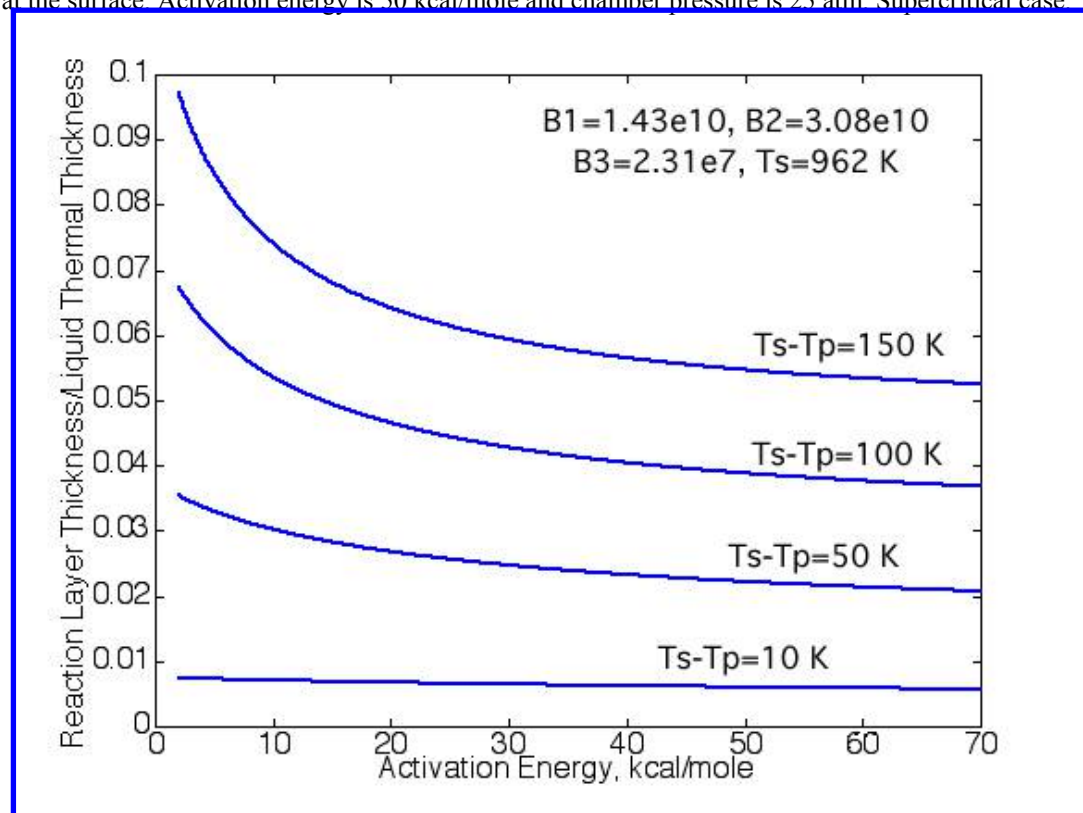
Figure 9: Reaction layer thickness relative to the characteristic thickness of the liquid as a function of the activation energy for several temperature differences evaluated at the surface and the start of the pyrolysis zone.

36
American Institute of Aeronautics and Astronautics
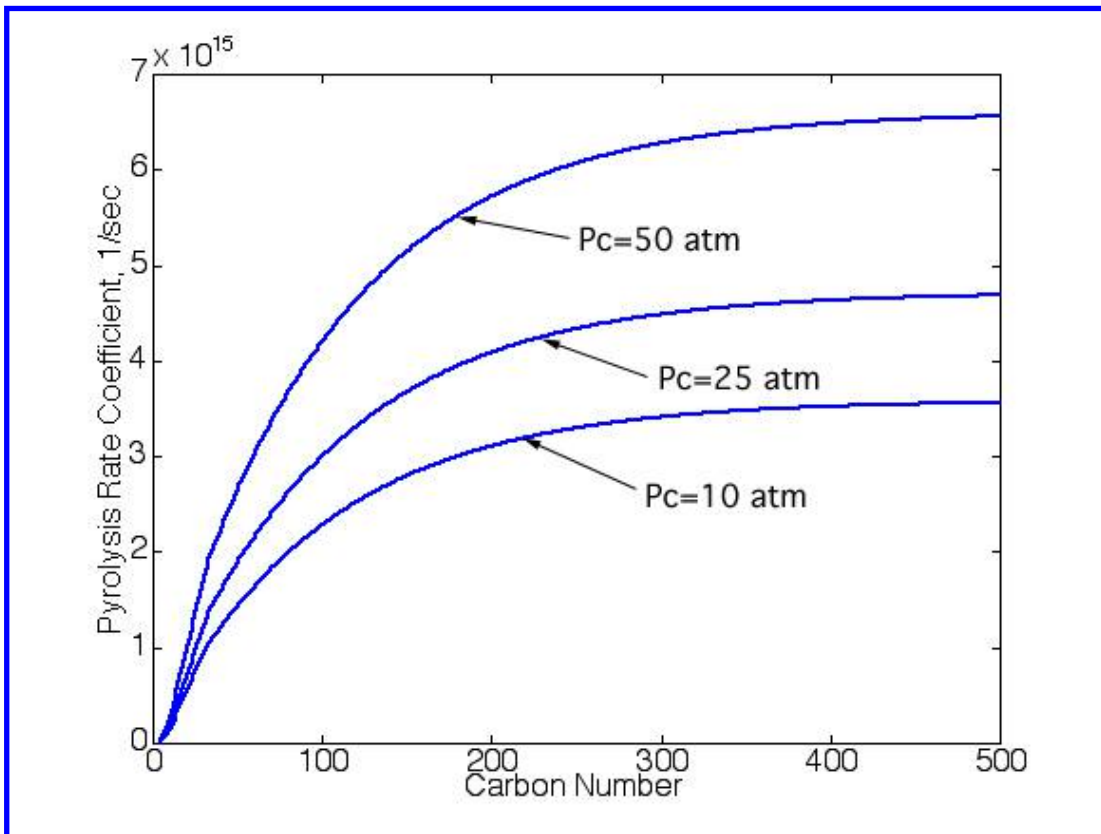
Figure 10: The pyrolysis rate coefficient for the n-alkanes as a function of the carbon number has been plotted for three pressure levels.
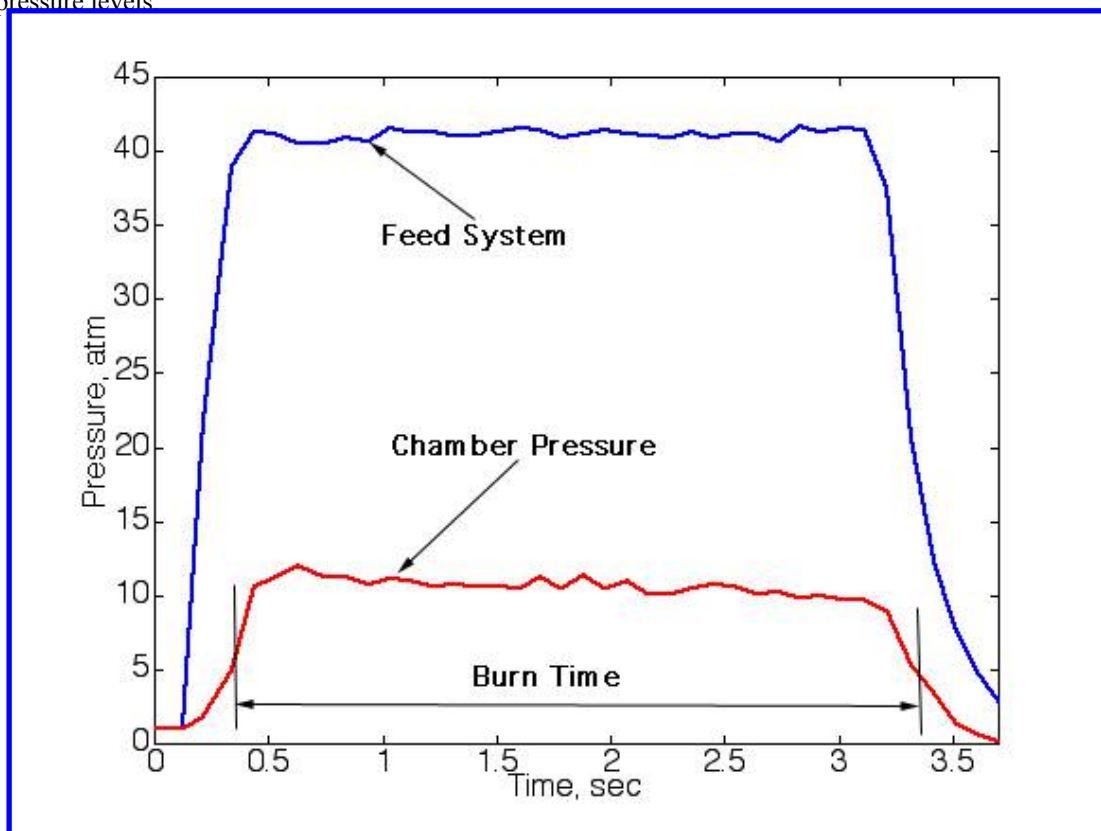
Figure 11: The Chamber and feed pressures for a typical test.
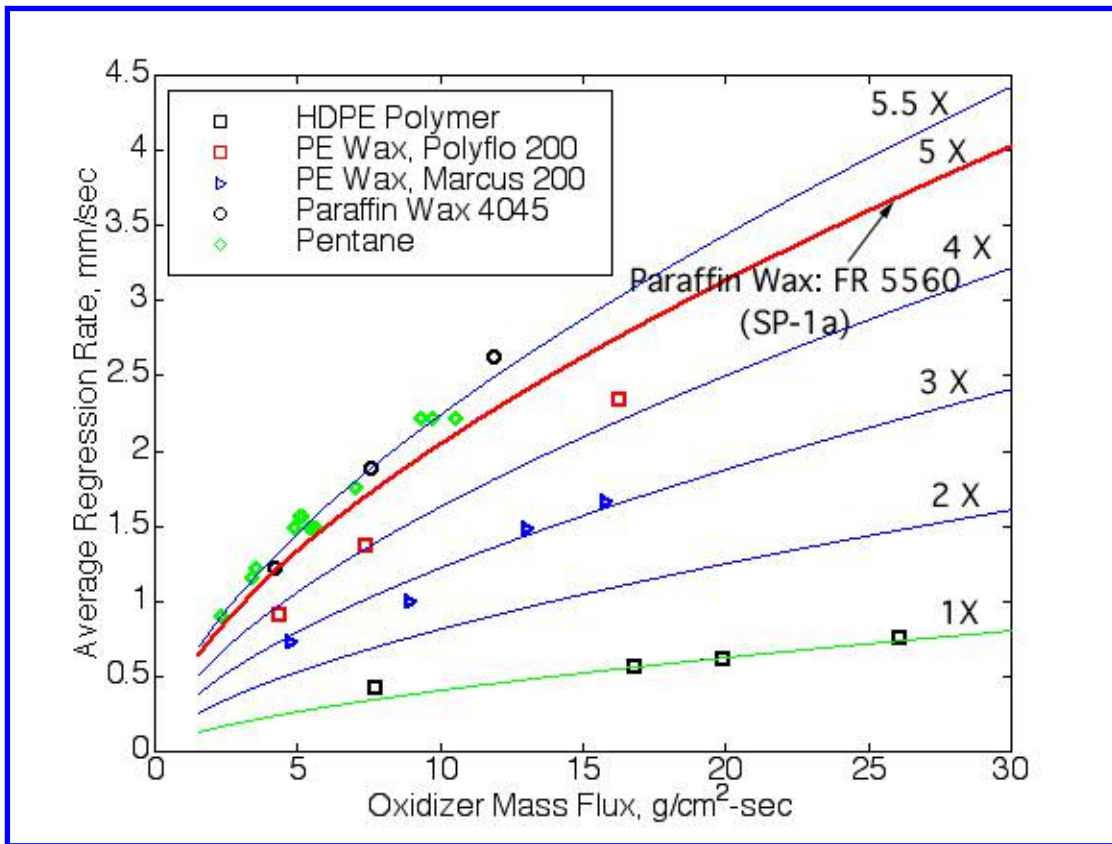
Figure 12: The regression rate data for the fuels considered in this paper
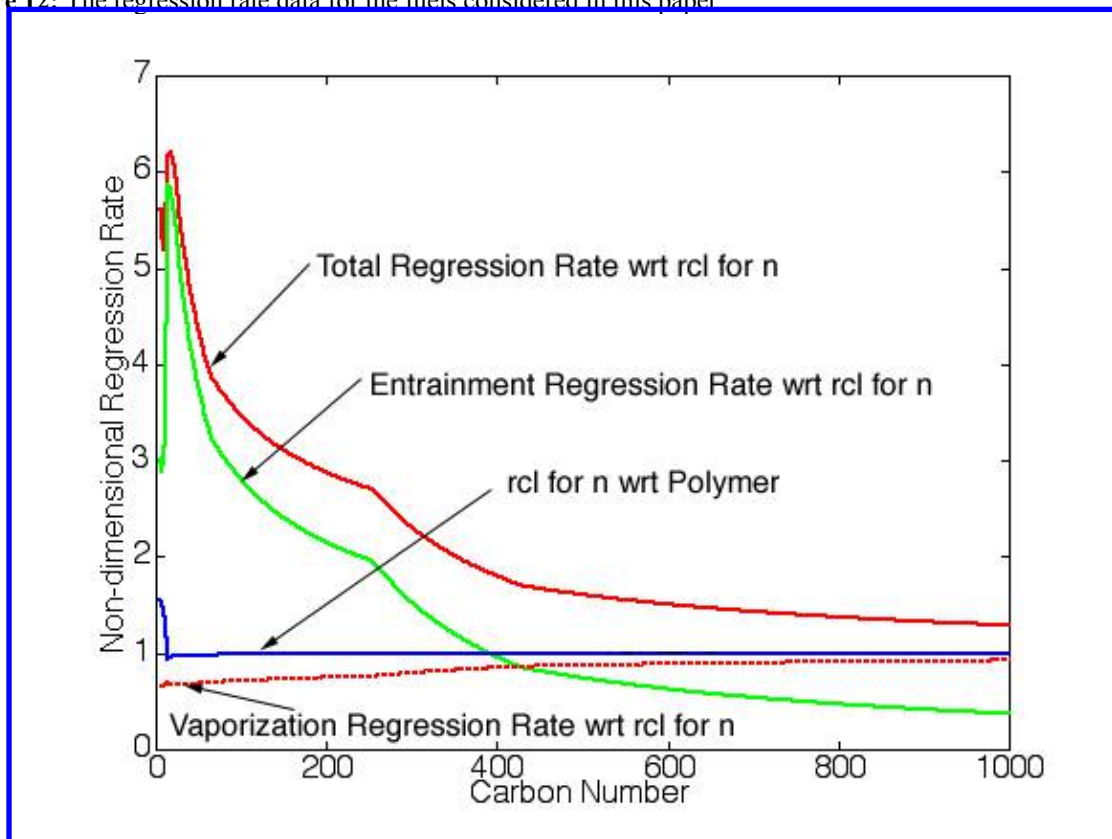
Figure 13: The non-dimensional regression rates for the series of n-alkanes as predicted by the liquid layer combustion theory.
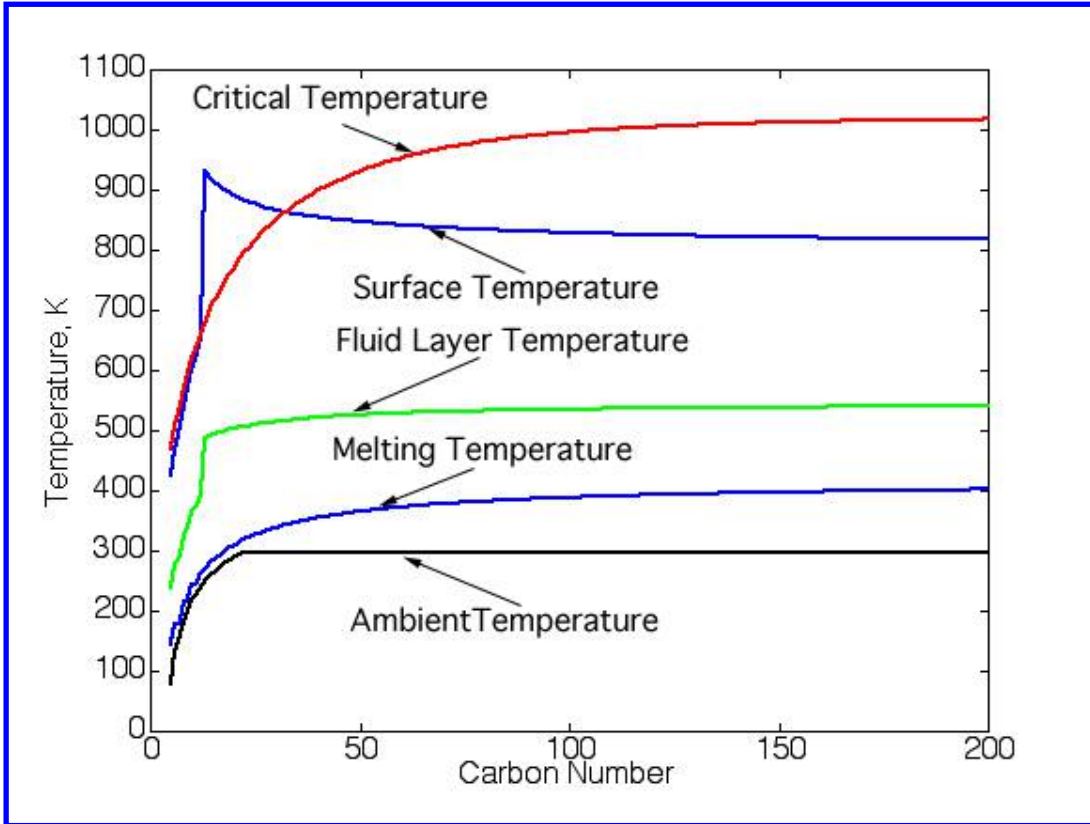
Figure 14: The temperature field in the condensed phase as a function of the carbon number for n-alkanes.
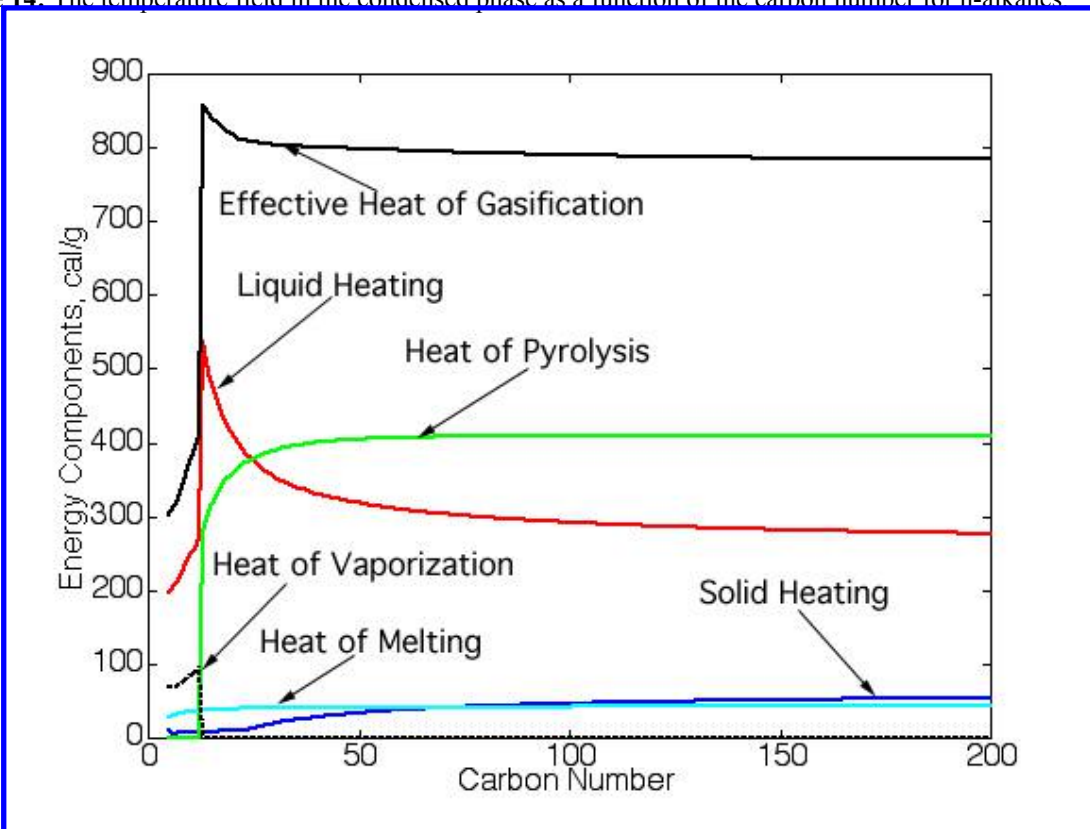
Figure 15: Effective heat of gasification and its components for the series of n-alkanes.
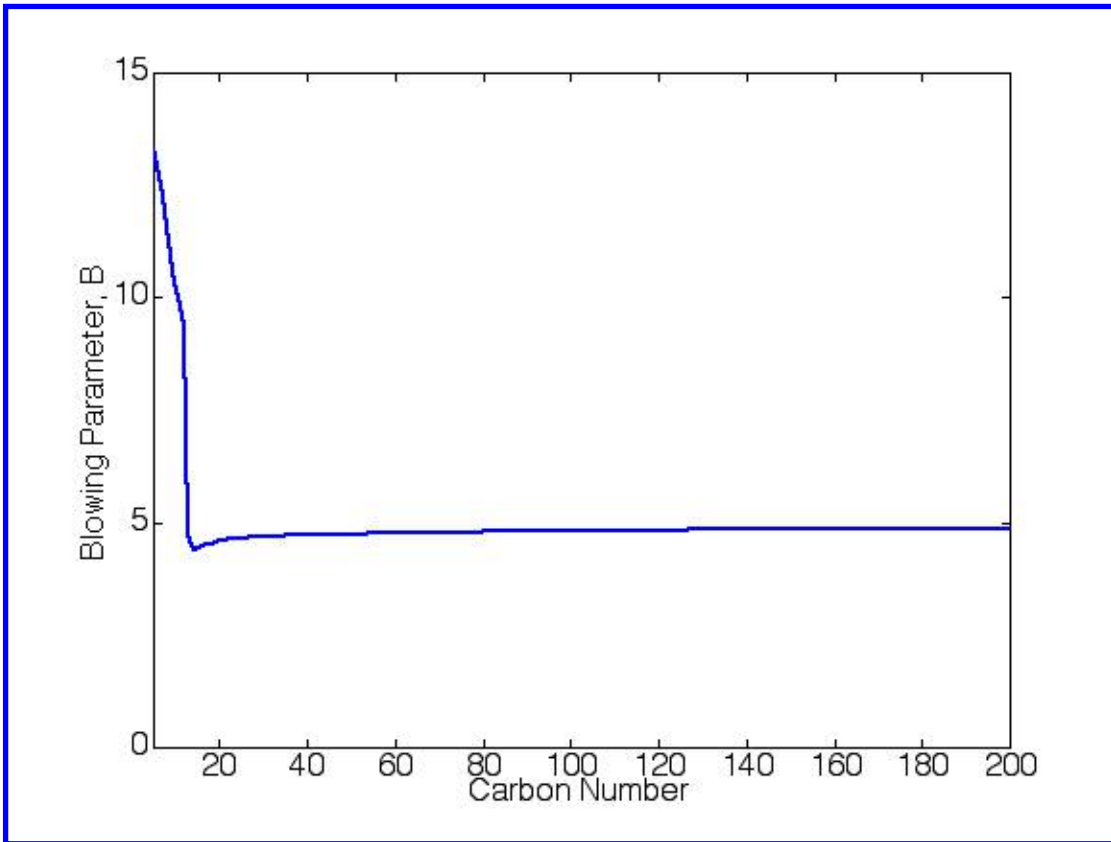
Figure 16: The blowing parameter for the series of n-alkanes.
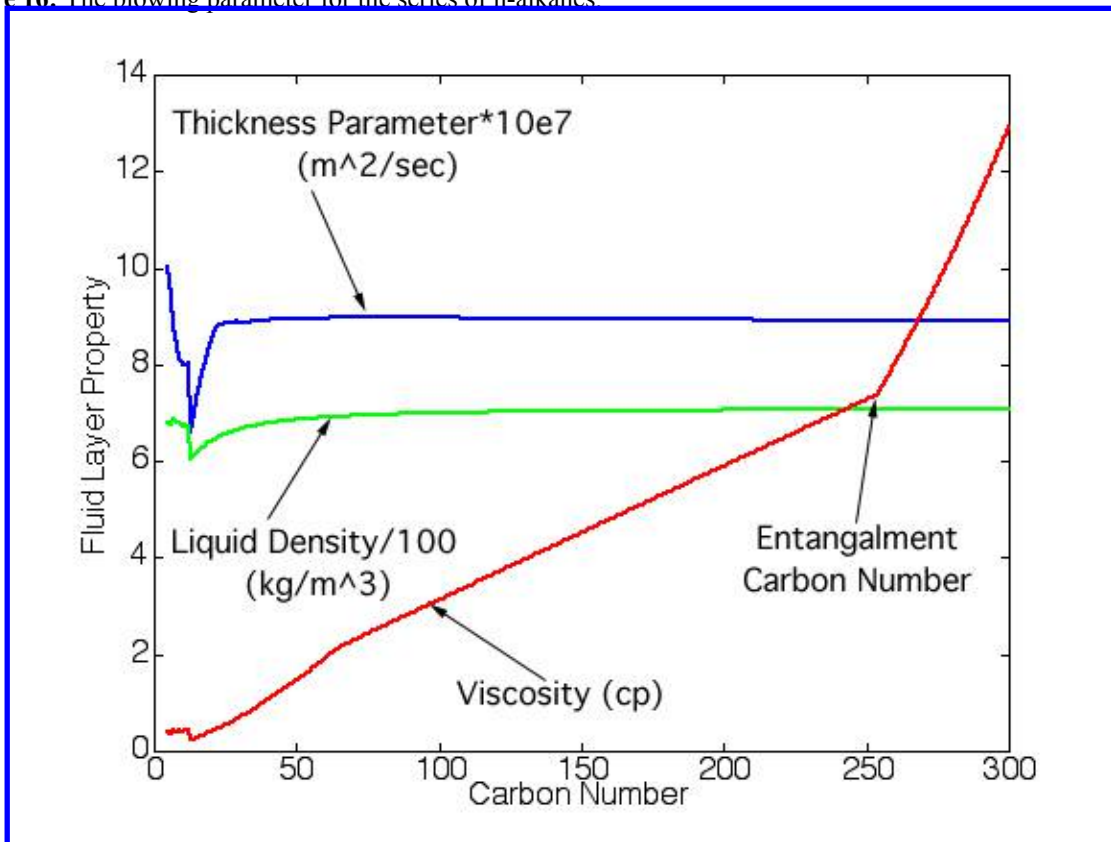
Figure 17: The viscosity, liquid density and thickness parameters evaluated at the effective fluid temperature for the series of n-alkanes.
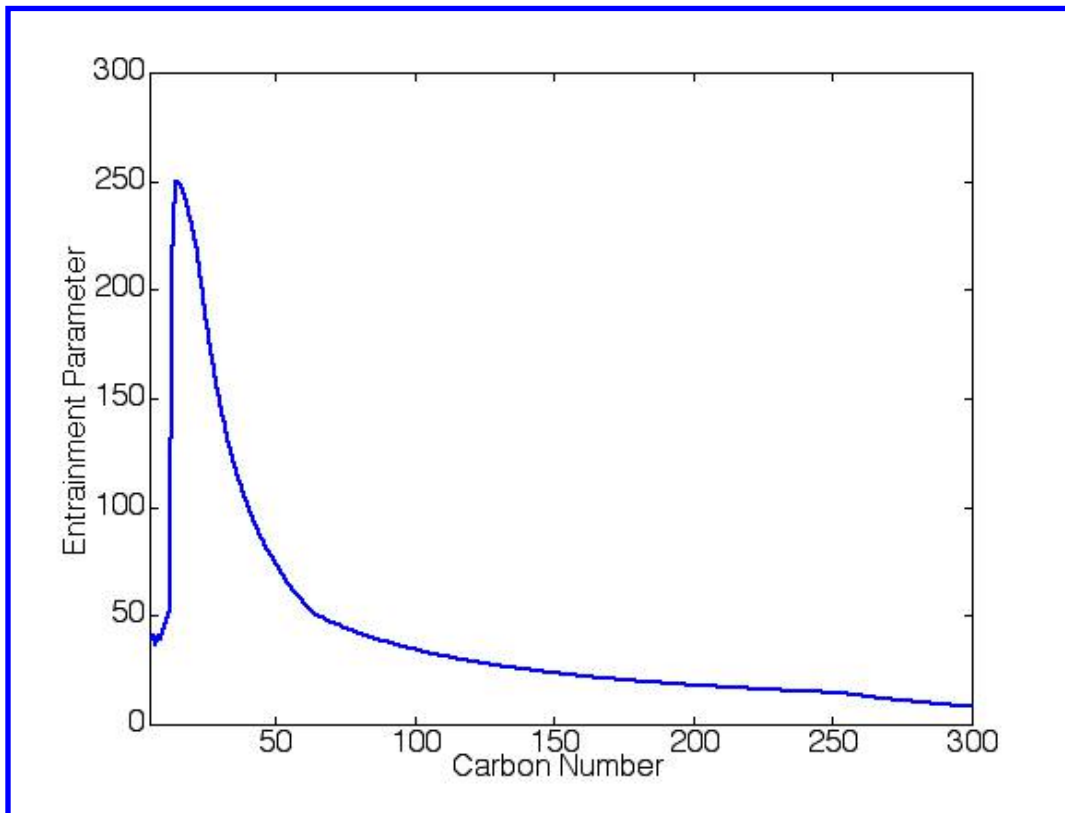
**Figure 18:** The entrainment parameter, R_{ent} for the series of n-alkanes.
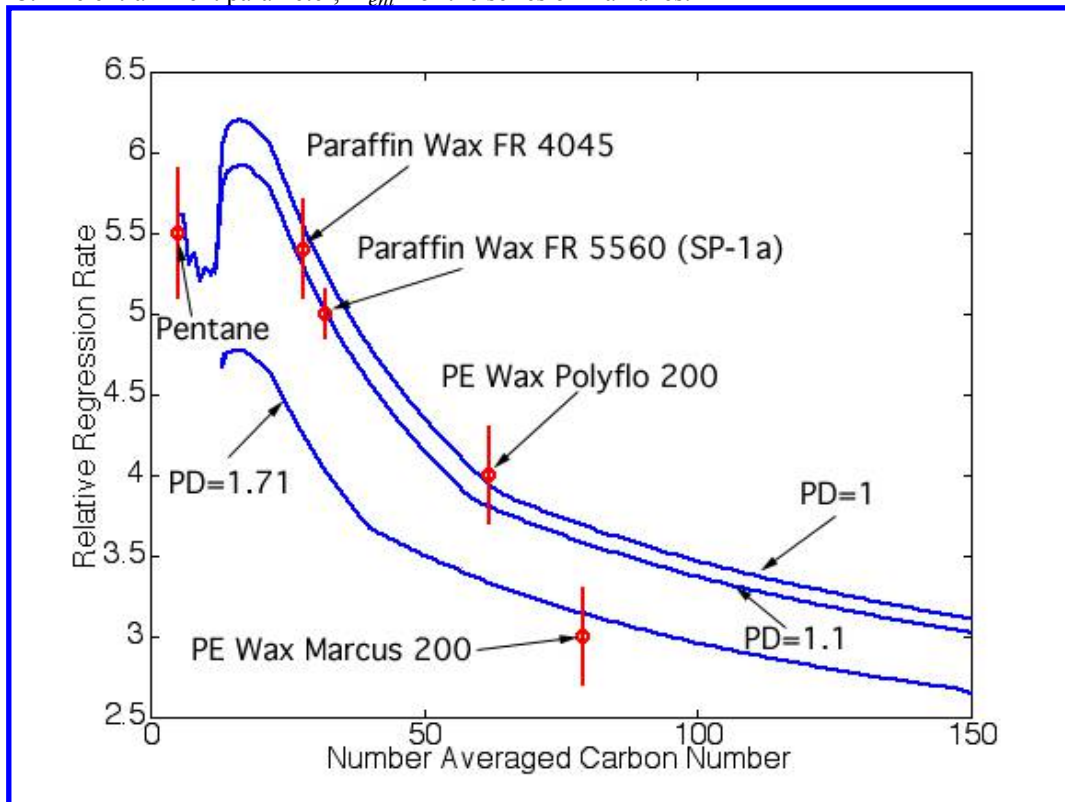
Figure 19: The regression rates of n-alkanes with respect to the regression rate of the HDPE polymer. Three plots corresponding three different polydipersity values have been produced. The experimental regression rate data for various paraffinic fuel have also been included in the figure.
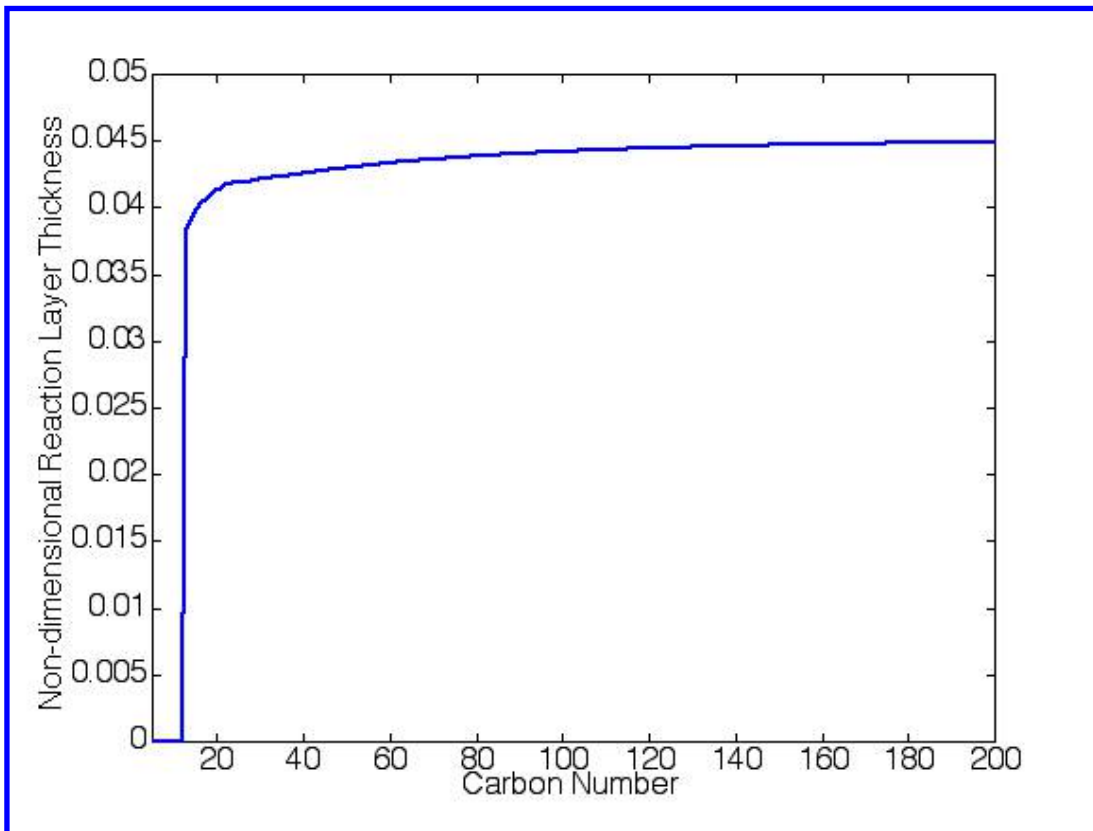
Figure 20: The thickness of the pyrolysis layer with respect to the characteristic thickness of the liquid layer as a function of carbon number for the series of n-alkanes has been plotted.
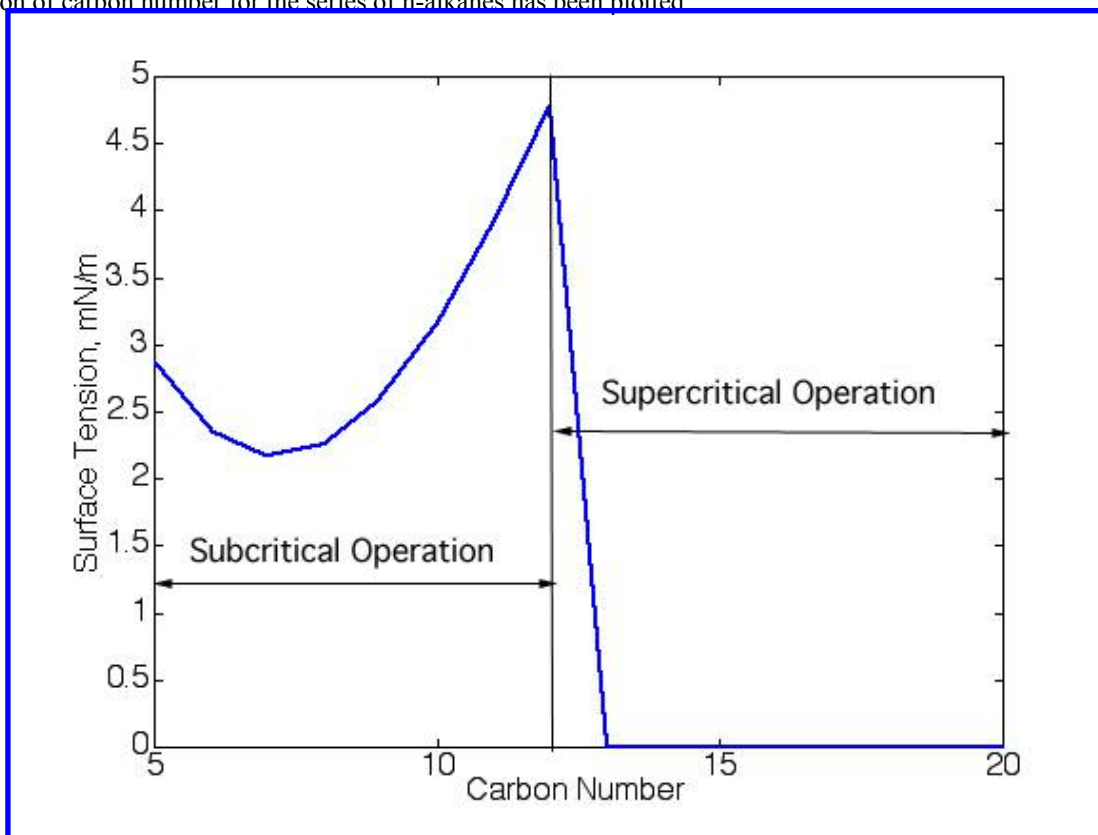
Figure 21: The surface tension as a function of the carbon number for chamber pressure of 20 atm.

This article has been cited by:

1. Maria Regina Apodaca Moreno, Javier K. Stober, Danielle Wood. Passive Method for Wax Casting in the Production of the Fuel Grain for in-space Hybrid Rocket . [Abstract] [PDF] [PDF Plus]

2. Lorenzo Casalino, Andrea Ferrero, Filippo Masseni, Luca Muscarà, Dario Pastrone, Maria Luisa Frezzotti, Adriano Annovazzi, Attilio Cretella, Rocco Carmine Pellegrini, Enrico Cavallini. Multiphysics modelling for a hybrid rocket engine with liquefying fuel: a sensitivity analysis on combustion instability . [Abstract] [PDF] [PDF Plus]

3. Giuseppe Gallo, Raffaele Savino. 2022. Regression Rate Model Assessed by Ballistic Reconstruction Technique in Hybrid Rocket Engines Burning Liquefying Fuels. *Aerospace Science and Technology* 107712. [Crossref]

4. Ştefan Predoi, Ştefan Grigorean, Gheorghe Dumitraşcu. 2022. The Regression Rate-Based Preliminary Engineering Design of Hybrid Rocket Combustion System. *Processes* 10:4, 775. [Crossref]

5. Keith Javier Stober, M. Regina Apodaca M., Danielle Wood. Paraffin & Beeswax Spaceflight Experiments for Improved Understanding of Centrifugal Casting 1-8. [Crossref]

6. Ozan Kara, Arif Karabeyoglu. Hybrid Propulsion System: Novel Propellant Design for Mars Ascent Vehicles . [Crossref]

7. Giuseppe Gallo, Stefano Mungiguerra, Raffaele Savino. 2021. New Entrainment Model for Modelling the Regression Rate in Hybrid Rocket Engines. *Journal of Propulsion and Power* 37:6, 893-909. [Abstract] [Full Text] [PDF] [PDF Plus]

8. Riccardo Bisin, Alberto Verga, Daniele Bruschi, Christian Paravan. Strategies for Paraffin-based Fuels Reinforcement: 3D Printing and Blending with Polymers . [Abstract] [PDF] [PDF Plus]

9. Gladys C. Ngetich, Keith Javier Stober, Danielle Wood. Numerical Simulation of Centrifugal Casting of Paraffin Wax: Influence of Rotational Speed and Fluid Viscosity . [Abstract] [PDF] [PDF Plus]

10. Genya Naka. Numerical Model of Radiative and Convective Heat Flux for Fuel Regression Rate of Wax-based Hybrid Rocket . [Abstract] [PDF] [PDF Plus]

11. Yuki FUNAMI, Keisuke UCHISHIMA, Shota HOMME, Sayaka NISHINO, Atsushi TAKANO. 2021. Evaluation of Hybrid Rocket Fuel Grain with a Star Fractal Port Using Combustion Experiments. *TRANSACTIONS OF THE JAPAN SOCIETY FOR AERONAUTICAL AND SPACE SCIENCES, AEROSPACE TECHNOLOGY JAPAN* 19:3, 295-303. [Crossref]

12. Mario Tindaro Migliorino, Daniele Bianchi, Francesco Nasuti. 2020. Numerical Analysis of Paraffin-Wax/Oxygen Hybrid Rocket Engines. *Journal of Propulsion and Power* 36:6, 806-819. [Abstract] [Full Text] [PDF] [PDF Plus]

13. Isabelle C. Sanders, Fabio A. Bendana, China Hagstrom, Raymond M. Spearrin. Assessing Oxidizer Injector Design via Thermochemical Imaging of PMMA Combustion in a Hybrid Rocket Motor Geometry . [Abstract] [PDF] [PDF Plus]

14. Benoit Dequick, Michel Lefebvre, Patrick Hendrick. CFD Simulation of a 1kN Paraffin-fueled Hybrid Rocket Engine . [Abstract] [PDF] [PDF Plus]

15. Genya Naka, Jerome Messineo, Koki Kitagawa, Carmine Carmicino, Toru Shimada. Prediction of Space and Time Distribution of Wax-based Fuel Regression Rate in a Hybrid Rocket . [Abstract] [PDF] [PDF Plus]

16. Elizabeth T. Jens, Ashley C. Karp, Victor A. Miller, G. Scott Hubbard, Brian J. Cantwell. 2020. Experimental Visualization of Hybrid Combustion: Results at Elevated Pressures. *Journal of Propulsion and Power* 36:1, 33-46. [Abstract] [Full Text] [PDF] [PDF Plus]

17. Taira Ishigaki, Ichiro Nakagawa. 2020. Improving Physical Properties of Wax-Based Fuels and Its Effect on Regression Rate. *Journal of Propulsion and Power* 36:1, 123-128. [Abstract] [Full Text] [PDF] [PDF Plus]

18. Yuki FUNAMI, Atsushi TAKANO. 2020. Averaged Regression Rate Evaluation of Hybrid Rocket Fuel Grain with a Star Fractal Port. *AEROSPACE TECHNOLOGY JAPAN, THE JAPAN SOCIETY FOR AERONAUTICAL AND SPACE SCIENCES* 19:0, 91-100. [Crossref]

19. Anna Petrarolo, Alexander Ruettgers, Mario Kobald. Data Clustering of Hybrid Rocket Combustion Flame . [Citation] [PDF] [PDF Plus]

20. Fabio A. Bendana, Josue J. Castillo, China G. Hagström, Raymond M. Spearrin. Thermochemical structure of a hybrid rocket reaction layer based on laser absorption tomography . [Citation] [PDF] [PDF Plus]

21. Giuseppe Daniele Di Martino, Carmine Carmicino, Stefano Mungiguerra, Raffaele Savino. 2019. The Application of Computational Thermo-Fluid-Dynamics to the Simulation of Hybrid Rocket Internal Ballistics with Classical or Liquefying Fuels: A Review. *Aerospace* 6:5, 56. [Crossref]

22. Enrico Paccagnella, Marco Santi, Alessandro Ruffin, Francesco Barato, Daniele Pavarin, Gianluigi A. Misté, Giovanni Venturelli, Nicolas Bellomo. 2019. Testing of a Long-Burning-Time Paraffin-Based Hybrid Rocket Motor. *Journal of Propulsion and Power* 35:2, 432-442. [Abstract] [Full Text] [PDF] [PDF Plus]

23. D. Bianchi, F. Nasuti, D. Delfini. Modeling of gas–surface interface for paraffin-based hybrid rocket fuels in computational fluid dynamics simulations 3-24. [Crossref]

24. Takashi SAKURAI, Yuya OISHIGE, Kazuyuki SAITO. 2019. Fuel regression behavior of swirling-injection end-burning hybrid rocket engine. *Journal of Fluid Science and Technology* 14:3, JFST0025-JFST0025. [Crossref]

25. Goutham Karthikeyan, Toru Shimada. 2018. Numerical Parametric Analysis of Combustion Instability in Axial-Injected Hybrid Rocket Motors. *Journal of Propulsion and Power* 34:6, 1542-1552. [Abstract] [Full Text] [PDF] [PDF Plus]

26. Enrico Paccagnella, Francesco Barato, Riccardo Gelain, Daniele Pavarin. CFD Simulations of Self-pressurized Nitrous Oxide Hybrid Rocket Motors . [Citation] [PDF] [PDF Plus]

27. Anna Petrarolo, Mario Kobald, Stefan Schlechtriem. Visualization of Combustion Phenomena in Paraffin-Based Hybrid Rocket Fuels at Super-Critical Pressures . [Citation] [PDF] [PDF Plus]

28. Yuto Koinuma, Ichiro Nakagawa. Study on Effect of Radiation Heat Transfer to Regression Rate of Wax Fuel Hybrid Rocket . [Citation] [PDF] [PDF Plus]

29. Anna Petrarolo, Mario Kobald, Stefan Schlechtriem. 2018. Understanding Kelvin–Helmholtz instability in paraffin-based hybrid rocket fuels. *Experiments in Fluids* 59:4. . [Crossref]

30. G. D. Di Martino, C. Carmicino, R. Savino. 2017. Transient Computational Thermofluid-Dynamic Simulation of Hybrid Rocket Internal Ballistics. *Journal of Propulsion and Power* 33:6, 1395-1409. [Abstract] [Full Text] [PDF] [PDF Plus]

31. M. Kobald, C. Schmierer, H. K. Ciezki, S. Schlechtriem, E. Toson, L. T. De Luca. 2017. Viscosity and Regression Rate of Liquefying Hybrid Rocket Fuels. *Journal of Propulsion and Power* 33:5, 1245-1251. [Abstract] [Full Text] [PDF] [PDF Plus]

32. Nikita V. Muravyev, Konstantin A. Monogarov, Dmitry Prokopyev, Anatoly A. Bragin, Luciano Galfetti, Luigi T. DeLuca, Alla N. Pivkina. 2017. Macro- vs Microcrystalline Wax: Interplay of Evaporation and Decomposition under Pressure Variation. *Energy & Fuels* 31:8, 8534-8539. [Crossref]

33. Giuseppe Leccese, Daniele Bianchi, Francesco Nasuti, Keith J. Stober, Pavan Narsai, Brian J. Cantwell. Simulations of Paraffin-Based Hybrid Rocket Motors and Comparison with Experiments . [Citation] [PDF] [PDF Plus]

34. Anna Petrarolo, Mario Kobald, Stefan Schlechtriem. Liquid Layer Combustion Visualization of Paraffin-based Hybrid Rocket Fuels . [Citation] [PDF] [PDF Plus]

35. Marco Santi, Enrico Paccagnella, Alessandro Ruffin, Francesco Barato, Daniele Pavarin, Gianluigi Misté, Giovanni Venturelli, Nicolas Bellomo. Development and Testing of a Long Burning Time Lab-scale Paraffin-based Hybrid Rocket Motor . [Citation] [PDF] [PDF Plus]

36. Giuseppe D. Di Martino, Stefano Mungiguerra, Carmine Carmicino, Raffaele Savino. Computational Fluid-dynamic Simulations of Hybrid Rocket Internal Flow Including Discharge Nozzle . [Citation] [PDF] [PDF Plus]

37. Toru Shimada, Saburo Yuasa, Harunori Nagata, Shigeru Aso, Ichiro Nakagawa, Keisuke Sawada, Keiichi Hori, Masahiro Kanazaki, Kazuhisa Chiba, Takashi Sakurai, Takakazu Morita, Koki Kitagawa, Yutaka Wada, Daisuke Nakata, Mikiro Motoe, Yuki Funami, Kohei Ozawa, Tomoaki Usuki. Hybrid Propulsion Technology Development in Japan for Economic Space Launch 545-575. [Crossref]

38. Yogesh Kumar Sinha, B. T. N. Sridhar, R. Kishnakumar. 2016. Study of Thermo-Mechanical Properties of HTPB–Paraffin Solid Fuel. *Arabian Journal for Science and Engineering* 41:11, 4683-4690. [Crossref]

39. Elizabeth T. Jens, Brian J. Cantwell, G. Scott Hubbard. 2016. Hybrid rocket propulsion systems for outer planet exploration missions. *Acta Astronautica* 128, 119-130. [Crossref]

40. Giuseppe Leccese, Daniele Bianchi, Francesco Nasuti. Modeling of Paraffin-Based Fuels in the Simulation of Hybrid Rocket Flowfields . [Citation] [PDF] [PDF Plus]

41. Anna PETRAROLO, Mario KOBALD. 2016. Evaluation techniques for optical analysis of hybrid rocket propulsion. *Journal of Fluid Science and Technology* 11:4, JFST0028-JFST0028. [Crossref]

42. M. Lazzarin, M. Faenza, F. Barato, N. Bellomo, A. Bettella, D. Pavarin. 2015. Computational Fluid Dynamics Simulation of Hybrid Rockets of Different Scales. *Journal of Propulsion and Power* 31:5, 1458-1469. [Abstract] [Full Text] [PDF] [PDF Plus]

43. Mario Kobald, Anna Petrarolo, Stefan Schlechtriem. Combustion Visualization and Characterization of Liquefying Hybrid Rocket Fuels . [Citation] [PDF] [PDF Plus]

44. Omer Dermanci, Arif M. Karabeyoglu. Effect of Nano Particle Addition on the Regression Rate of Liquefying Fuels . [Citation] [PDF] [PDF Plus]

45. Masaki Adachi, Toru Shimada. 2015. Liquid Films Instability Analysis of Liquefying Hybrid Rocket Fuels Under Supercritical Conditions. *AIAA Journal* 53:6, 1578-1589. [Abstract] [Full Text] [PDF] [PDF Plus]

46. F. Barato, N. Bellomo, M. Faenza, M. Lazzarin, A. Bettella, D. Pavarin. 2015. Numerical Model to Analyze Transient Behavior and Instabilities on Hybrid Rocket Motors. *Journal of Propulsion and Power* **31**:2, 643-653. [Abstract] [Full Text] [PDF] [PDF Plus]

47. Mario Kobald, Isabella Verri, Stefan Schlechtriem. 2015. Theoretical and experimental analysis of liquid layer instability in hybrid rocket engines. *CEAS Space Journal* **7**:1, 11-22. [Crossref]

48. M. Lazzarin, M. Faenza, F. Barato, N. Bellomo, A. Bettella. 2015. Numerical Simulation of Hybrid Rockets Liquid Injection and Comparison with Experiments. *Journal of Propulsion and Power* **31**:1, 352-364. [Abstract] [Full Text] [PDF] [PDF Plus]

49. S. C. Shark, C. R. Zaseck, T. L. Pourpoint, S. F. Son. 2014. Solid-Fuel Regression Rates and Flame Characteristics in an Opposed Flow Burner. *Journal of Propulsion and Power* **30**:6, 1675-1682. [Abstract] [Full Text] [PDF] [PDF Plus]

50. Yuki Funami, Toru Shimada. Combined Analysis of Reactive Flow and Heat Transfer for Hybrid Rocket Design Engineering . [Citation] [PDF] [PDF Plus]

51. Masaki Adachi, Toru Shimada. Instability Analysis of Liquid Films of Liquefying Hybrid Rocket Fuels under Supercritical Operating Condition . [Citation] [PDF] [PDF Plus]

52. Nicolas Bellomo, Marta Lazzarin, Francesco Barato, Alberto Bettella, Daniele Pavarin, Matthias Grosse. 2014. Investigation of Effect of Diaphragms on the Efficiency of Hybrid Rockets. *Journal of Propulsion and Power* **30**:1, 175-185. [Abstract] [Full Text] [PDF] [PDF Plus]

53. Mario Kobald, Helmut Ciezki, Stefan Schlechtriem. Optical Investigation of the Combustion Process in Paraffin-based Hybrid Rocket Fuels . [Citation] [PDF] [PDF Plus]

54. Nicolas Gascoin. Kinetic Modelling of High Density PolyEthylene Pyrolysis: Part 2. Reduction of existing detailed mechanism . [Citation] [PDF] [PDF Plus]

55. Nicolas Gascoin. Firing tests of hybrid engine with varying oxidizer nature and operating conditions . [Citation] [PDF] [PDF Plus]

56. Nicolas Gascoin. Micro and Full-Scale Experiments on Hybrid Rocket Fuel and Prelude to Hybrid Rocket Combustor Simulations . [Citation] [PDF] [PDF Plus]

57. Yuki FUNAMI, Toru SHIMADA. 2013. Validation of Integral Method for Numerical Prediction of Hybrid Rocket Internal Ballistics. *Journal of Fluid Science and Technology* **8**:2, 172-185. [Crossref]

58. Francesco Barato, N. Bellomo, M. Lazzarin, F. Moretto, Alberto Bettella, Daniele Pavarin. Numerical Modeling of Paraffin-Based Fuels Behavior . [Citation] [PDF] [PDF Plus]

59. Kenneth Kuo, Ryan Houim. Theoretical Modeling and Numerical Simulation Challenges of Combustion Processes of Hybrid Rockets . [Citation] [PDF] [PDF Plus]

60. Matthias Grosse. Effect of a Diaphragm on Performance and Fuel Regression of a Laboratory Scale Hybrid Rocket Motor Using Nitrous Oxide and Paraffin . [Citation] [PDF] [PDF Plus]

61. Matthias Grosse, Gerhard Schlatzke. Development of a Hybrid Rocket Motor Using a Diaphragm for a Small Test Rocket . [Citation] [PDF] [PDF Plus]

62. . Combustion Instability and Transient Behavior in Hybrid Rocket Motors 351-412. [Citation] [PDF] [PDF Plus]

63. . Review of Solid-Fuel Regression Rate Behavior in Classical and Nonclassical Hybrid Rocket Motors 37-126. [Crossref]

64. C. Carmicino, A. Russo Sorge. 2006. Influence of a Conical Axial Injector on Hybrid Rocket Performance. *Journal of Propulsion and Power* **22**:5, 984-995. [Citation] [PDF] [PDF Plus]